Aerosol Res., 4, 457–483, 2026
https://doi.org/10.5194/ar-4-457-2026
© Author(s) 2026. This work is distributed under
the Creative Commons Attribution 4.0 License.

AEROSOL Research
Open Access

Drivers governing the seasonality of new particle formation in the Arctic

Dominic Heslin-Rees[1,2], Peter Tunved[1,2], Diego Aliaga[1], Janne Lampilahti[3], Ilona Riipinen[1,2], Annica M. L. Ekman[4,2], Ki-Tae Park[5], Martina Mazzini[6], Stefania Gilardoni[7], Roseline Thakur[3], Kihong Park[8], Young Jun Yoon[9], Kitack Lee[10], Mikko Sipilä[3], Mauro Mazzola[11], and Radovan Krejci[1,2]

[1]Department of Environmental Science (ACES), Stockholm University, Stockholm, Sweden
[2]Bolin Centre for Climate Research, Stockholm University, Stockholm, Sweden
[3]Institute for Atmospheric and Earth System Research (INAR), Helsinki, Finland
[4]Department of Meteorology, Stockholm University, Stockholm, Sweden
[5]Department of Environmental Sciences and Biotechnology, Hallym University, Chuncheon, Gangwon, Republic of Korea
[6]Institute of Atmospheric Science and Climate (CNR-ISAC), Bologna, Italy
[7]Institute of Polar Sciences (CNR-ISP), Milan, Italy
[8]School of Earth Sciences and Environmental Engineering, Gwangju Institute of Science and Technology, Buk-gu, Gwangju, Republic of Korea
[9]Korea Polar Research Institute, Yeonsu-gu, Incheon, Republic of Korea
[10]Division of Environmental Science and Engineering, Pohang University of Science and Technology, Pohang, Republic of Korea
[11]Institute of Polar Sciences, National Research Council (CNR-ISP), Bologna, Italy

Correspondence: Dominic Heslin-Rees (dominic.heslin-rees@aces.su.se) and Radovan Krejci (radovan.krejci@aces.su.se)

Received: 2 March 2025 – Discussion started: 19 March 2025
Revised: 4 September 2026 – Accepted: 4 September 2026 – Published: 6 October 2026

Abstract. New particle formation (NPF) is the phenomenon wherein gaseous precursors form critical clusters of barely a few nanometres in diameter, after which, under favourable conditions, these particles can grow to climate-relevant sizes. Here we present measurements from 2022 to 2024 of particle and ion number size distributions from the Zeppelin Observatory (ZEP), an Arctic research station situated on the western edge of Svalbard atop a mountain. NPF events begin in April and continue occurring into November. The events at the start of the NPF season (i.e. April/May) are considerably stronger (i.e. a larger production of nucleation mode particles) compared with other months of the year. The peaks in NPF strength coincide with peaks in the accumulated solar insolation experienced by arriving air masses. During the summer period NPF events occur on 20 %–40 % of days each month; however, there is a consistent decline starting in June. We show that the combined influence of solar insolation and the surface area of pre-existing aerosols (i.e. condensation sink, CS) is a strong predictor for the likelihood of NPF. We develop a simplified predictive model which matches the frequency of NPF events identified via the classification schemes used in this study; we show that the ratio of solar insolation over CS corresponds well to the frequency of NPF events (R^2 of 0.78). We show that NPF events occur during the polar night (i.e. when the sun does not pass above the horizon) and that these events are linked to high-altitude air masses. Furthermore, we detail the likely geographic origins of nucleation mode particles as measured at ZEP. We show that NPF events are considerably more likely to originate from marine regions towards the west of Svalbard, particularly the Greenland Sea, which is the marine region with the greatest likelihood of originating air masses linked to an NPF day. We also show that NPF events lead to an increase in the number of Aitken mode particles, indicating that potentially a significant proportion of the Aitken mode particles originate from NPF. Of

the measured NPF events, 37 % exhibited nucleation mode particles that grew beyond 25 nm (a diameter representing the minimum activation diameter for particles to act as cloud condensation nuclei). Overall, we present a concise picture of the life cycle of nucleation mode particles in the Arctic, including the effect wet scavenging has in reducing the condensation sink, which in turn promotes the occurrence of NPF events.

1 Introduction

New particle formation (NPF) describes the production of secondary aerosol particles from precursor gases to clusters of molecules a few nanometres in diameter. Newly formed particles belong to the nucleation mode (i.e. typically < 10 nm) and may grow through the continued coagulation and condensation of vapours into Aitken mode particles (i.e. tens of nanometres in diameter). The phenomenon of NPF has been observed globally (Kerminen et al., 2018); however, in each region the chemical characteristics and controlling source and sink processes leading to NPF may vary.

Arctic aerosol seasonality is governed by a combination of atmospheric general circulation; meteorology; and several source and sink processes including the direct emission of local primary particles, NPF, the long-range transport of anthropogenic emissions from lower latitudes, and the removal of particles through wet scavenging (Garrett et al., 2011; Schmale et al., 2022; Tunved et al., 2013; Willis et al., 2018). One distinctive feature of the annual cycle is the Arctic haze in late winter and early spring, which is characterised by a sustained increase in the number of accumulation mode aerosols (i.e. particles typically around 100 nm) (e.g. Shaw, 1995). Reduced wet scavenging and increased transport efficiency from anthropogenic source regions at lower latitudes during this part of the year give rise to this phenomenon (Garrett et al., 2011). The Arctic summertime, by contrast, is less influenced by long-range-transported pollutants, and the increased precipitation effectively reduces the once pronounced accumulation mode. Moreover, increased photochemistry and biological activity (e.g. phytoplankton blooms) provide a source of precursor gases encouraging NPF and the growth of newly formed particles (Tunved et al., 2013; Croft et al., 2016; Price et al., 2023); as a result, the smaller Aitken and ultrafine aerosol particles increase in number.

Changes in aerosol size, abundance, and chemical composition can perturb the radiative balance either indirectly by acting as cloud condensation nuclei (CCN), altering cloud formation, brightness, and lifetime, or directly through their interaction with both short- and long-wave radiation (Li et al., 2022). The Arctic region can at times be CCN-limited, which means that small changes in CCN concentrations could potentially impact cloud properties via cloud-mediated indirect aerosol effects, which in this and similar environments could result in surface warming due to enhanced long-wave cloud forcing (Garrett et al., 2004; Garrett and Zhao, 2006; Mauritsen et al., 2011). Thus, local–regional-scale production of aerosols during the summertime and changes to this production mechanism may have significant consequences for the Arctic (Kecorius et al., 2019). Still however, the impact of newly formed particles on Arctic cloud properties remains poorly quantified.

Newly formed particles can reach climate-relevant sizes; however, this depends on certain factors, e.g. the production and volatility of condensable vapours and the condensation and coagulation sinks. In the Arctic, particles as small as 25 nm have been shown to act as CCN (Leaitch et al., 2016; Karlsson et al., 2020, 2021; Pöhlker et al., 2021; Gramlich et al., 2023; Motos et al., 2023), thereby helping to form clouds and potentially influencing their radiative properties and lifetime. Motos et al. (2023) predicted a similar lower limit for activation diameters of 20 nm; however, they suggested that the summertime NPF-derived Aitken mode may remain interstitial (inactivated). Other studies indicate that NPF produces a substantial fraction of Arctic CCN (Gordon et al., 2017; Merikanto et al., 2009).

Air ions are an additional focus area of aerosol effects, as they can play a role in nucleation (Hirsikko et al., 2011; Kirkby et al., 2011) and can influence aerosol particles through their formation and growth mechanism. Both positive and negative ions contribute to the production of newly formed particles in the Arctic, via ion-induced nucleation (see Beck et al., 2021, for negative ions and Jokinen et al., 2018, for positive ions) The overall contribution of ions to NPF is disputed as quantifying their impact on nucleation rates in ambient conditions remains difficult. However, studies suggest that the dynamics of sub-2 nm clusters is dominated by neutral clusters (Hirsikko et al., 2011; Kulmala et al., 2013). Ions can help stabilise clusters which form initially (Yu and Turco, 2001), with most particles formed from ion-induced nucleation reaching neutrality after growing beyond 2.5 nm (Wagner et al., 2017).

Observations of ultrafine particles ($\sim$ 3–20 nm) in the Arctic (onboard the Swedish icebreaker Oden, 70–85° N) were reported by Covert et al. (1996) and Wiedensohler et al. (1996). At Zeppelin Observatory (ZEP), Ström et al. (2003) and Tunved et al. (2013) presented measurements of small (> 10 nm) aerosol particles showing an increased concentration and frequency of formation events during the Arctic summer. Tunved et al. (2013) suggested that the summertime, coinciding with increased photochemical production of precursor gases and the removal of larger pre-existing aerosol, generates favourable conditions in which NPF can

occur. Other Arctic sites have been the focus of research into NPF, including Villum Research Station (hereafter Villum) (see Nguyen et al., 2016) and Summit (see Ziemba et al., 2010), both in Greenland, and Utqiaġvik, Alaska (Kolesar et al., 2017). Other studies, e.g. Brean et al. (2023), present NPF data from several locations, including Alert, Villum, Tiksi, ZEP, Gruvebadet (Ny-Ålesund), and Utqiaġvik; a commonality shared by all Arctic sites was the occurrence of NPF events during the summer and also that events coincided with air masses generally influenced by marine regions, including at Utqiaġvik and Alert, whereby a correlation was observed between biogenic methane sulfonate (MSA-) and summertime particle number concentrations (Leaitch et al., 2013; Quinn et al., 2002). Beck et al. (2021), through a comparison of measurements from both Ny-Ålesund and Villum, showed that different nucleation mechanisms can also occur at different times of the year at these two locations; at Villum iodic acid (IA; HIO_3) was found to be the primary driver of NPF events during springtime, and sulfuric acid (SA; H_2SO_4)–ammonium (AM; NH_3)-driven events were shown to occur in the summer. At Ny-Ålesund, NPF was driven by SA–AM during the springtime and highly oxygenated molecules (HOMs) during the summer. There is no evidence that anthropogenic precursors contribute to NPF at ZEP (Schmale and Baccarini, 2021). Instead, dimethyl sulfide (DMS), produced by phytoplankton, can serve as a precursor gas contributing to NPF. Marine regions with strong chlorophyll *a* concentrations and DMS production capacity have been linked to increased concentrations of nanoparticles, which suggests that marine biogenic sources are an important source of nucleating and condensing material (Lee et al., 2020). Observed DMS concentrations vary with air mass origin, season, and residence time over different marine source regions. For example, it has been shown that air masses exposed more to the Greenland Sea, compared with the Barents Sea, bring about higher DMS concentrations (Park et al., 2018). In the Arctic, there are low concentrations of nucleating agents as opposed to continental rural and urban locations (Karl et al., 2012; Pirjola et al., 2000). However, in spring and summer increased solar radiation, a lower total surface area of pre-existing particles (i.e. reduced condensation sink, CS), and coinciding phytoplankton blooms are shown to give rise to precursor gas concentrations sufficient to sustain ion-induced nucleation and growth of NPF-induced particles beyond 20 nm (Beck et al., 2021).

Recent modelling and global aerosol–climate coupling studies, both laboratory- and field-based, have increased our understanding of biogenic sulfur and iodine pathways. For sulfur pathways, Hoffmann et al. (2016) showed that the aqueous phase (i.e. cloud and aerosol water chemistry), not just the gas phase, plays an important role in the oxidation products of DMS, demonstrating the complexity of atmospheric sulfur chemistry in part due to the multiple oxidation pathways, which in turn are not represented well in climate models. Beyond sulfur-derived precursors, Finkenzeller et al. (2023) shed light on the formation mechanism for iodic acid (HIO_3) under atmospheric conditions and helped to corroborate how iodine can be produced and therefore act as a strong nucleating vapour in polar regions. Iodine-assisted NPF is also directly supported by the experimental findings shown in Baccarini et al. (2020). When iodine chemistry is included iodine acts as a missing source of low-volatility vapours and improves the modelled Aitken mode representation (Xavier et al., 2024).

In this study, we present 2.5 years' worth of measurements of particle and ion number size distributions, including three summer periods (total data coverage is from April 2022 to October 2024). Continuous measurements of sub-3 nm up to ∼ 850 nm particles were performed at the ZEP, Svalbard, providing unique information of the initial stages of nucleation and the subsequent growth. NPF events were identified, formation rates were calculated, and subsequent growth was analysed. The seasonality and coinciding environmental parameters encouraging NPF events and subsequent growth have been explored in detail. In this study, we offer a simplified approach to predicting the occurrence of NPF events, using proxies for the source and sink of newly formed particles, in a region with minimal anthropogenic influence particularly in the summertime, and also in a region where extensive measurement set ups are not always feasible.

2 Materials and methods

2.1 Measurement site

Zeppelin Observatory (ZEP) (78.90° N, 11.88°E; 474 m a.s.l.) is situated on the ridge of Mount Zeppelin, 2 km south from Ny-Ålesund research village on the western edge of the Norwegian Svalbard archipelago. ZEP represents regional background conditions in the Atlantic sector of the Arctic, as it is largely unaffected by local air pollution due to its location well above Ny-Ålesund and the prevailing wind patterns driven by Kongsfjorden's geography. ZEP is one of the most developed atmospheric observational sites in the Arctic, where a broad set of parameters has been measured for decades. It is part of numerous regional and global monitoring networks, including the Global Atmosphere Watch (WMO/GAW); Integrated Carbon Observation System (ICOS); the Aerosol, Clouds, and Trace Gases Research Infrastructure (ACTRIS); and the co-operative programme for monitoring and evaluation of the long-range transmission of air pollutants in Europe (EMEP). For a detailed description of the observatory, local meteorology and climatology, history, and observational programme see Platt et al. (2022).

2.2 Instrumentation

For this study, an array of instruments have been used to measure aerosol and ion size distributions between 0.8 and

850 nm including a neutral cluster and air ion spectrometer (NAIS5, Airel Ltd. Tartu, Estonia), a nanoparticle scanning mobility particle sizer (Nano SMPS, TSI), and a differential mobility particle sizer (DMPS) system. Particle and ion number size distributions and concentrations form the core data used in this study. Several other supporting data sets were used for data analysis and interpretation and are described below. This study covers the period from 17 April 2022 to 4 October 2024.

2.2.1 Differential mobility particle sizer (DMPS) system

Particle number size distributions, from 5 to 850 nm, were measured using a custom-made twin-DMPS system with a closed-loop sheath circulation and composed of two Hauke-type differential mobility analysers (DMAs). DMPS-1, with a short (5.3 cm) DMA, measured aerosol size distribution from 5 to 57 nm using a sample-to-sheath air ratio close to 1 : 10. DMPS-2, with a medium-length DMA (28 cm), measured size distribution from 20 to 850 nm using a sample-to-sheath air ratio close to 1 : 5. The aerosol particles were counted using condensational particle counters (CPCs) at a frequency of 1 Hz with the two CPCs. Particles > 3 nm were measured using the Ultrafine CPC (UCPC) TSI model 3776 (cut-off of 2.5 nm) coupled to the DMPS-1. Particles > 10 nm were measured with the CPC TSI model 3010 (cut-off of 10 nm) coupled to the DMPS-2. The two DMAs were run in a stepwise mode, providing two particle number size distribution cycles approximately every 27 min. The overlap between the size ranges measured by both DMPSs was used to check consistency and to merge both size distributions into one. Additional information can be found in Karlsson et al. (2021). The DMPS measurements were corrected for diffusional losses using the Particle Loss Calculator (PLC) according to von der Weiden et al. (2009) (see Fig. S1 in the Supplement for details).

2.2.2 Neutral Cluster and Air Ion Spectrometer (NAIS)

NAIS was utilised to measure concentrations of ions (charged particles and cluster ions) of both polarities between 0.8 and 40 nm and particles between 2.5 and 40 nm. The NAIS is an aerosol mobility spectrometer; when the sample is left unmodified it detects naturally charged ions and particles, and when the corona charger is used to charge the particle population it measures all particles, including the uncharged (Manninen et al., 2011; Mirme et al., 2007; Mirme and Mirme, 2013). It consists of 2 mobility analyser columns, with a total of 25 electrometers per column. Its lower size thresholds and high temporal resolution make it highly suitable for observing the early stages of NPF. The NAIS provides very accurate size information, regardless of the choice of the inversion algorithm used (in this case, the 25-channel V14.1 inverter algorithm) (Wagner et al., 2016). The lowest detection limit for the NAIS in particle mode is set based on the diameter of the corona charger ions and the inability of the electrical filter to remove all naturally charged particles (Manninen et al., 2011); however, there is a broad consensus that measurements of concentrations of particles below 2.5 nm are inaccurate.

The NAIS at ZEP was installed with a very short metallic inlet, less than 1m long, to minimise diffusional losses. The inlet pointed slightly downward, and a metallic rain shield was attached at the end to ensure that rain did not enter into the instrument. The NAIS inlet was heated to prevent ice blocking the inlet and also to limit water condensing inside the tubing. The NAIS was serviced and cleaned once a year. Additional aspects of the NAIS observations, including the apparent overestimation of particle number concentrations when compared to DMPS measurements (see also Kangasluoma et al., 2020) and the loss of negative cluster ions, can be found in Sect. S2.6 of the Supplement.

2.2.3 Complementary observations

A nanoparticle scanning mobility particle sizer (Nano SMPS, TSI), comprising a nano-differential mobility analyser (nano-DMA, TSI 3085, USA) and an ultrafine CPC (TSI 3776, USA), provided size distributions of nanoparticles (3–60 nm). See Lee et al. (2020) for further details. Atmospheric dimethyl sulfide (DMS) was measured using an analytical system in which DMS is trapped and eluted before being quantified using gas chromatography equipped with a pulsed-flame photometric detector. The detection limit is approximately 1.5 pptv given air samples of around 6 L. For more details, see Jang et al. (2016) and Park et al. (2018). Meteorological parameters including visibility, relative humidity, wind speed and direction, ambient temperature, and pressure were also further utilised throughout the study.

2.3 Data analysis of aerosol measurements

For processing of the NAIS data the *nais-processor* was used (https://github.com/jlpl/nais-processor, v0.0.30). The *nais-processor* Python package corrected for diffusional losses in the inlet (Gormley and Kennedy, 1948), applied an ion mode calibration (Wagner et al., 2016), converted ion mobility to particle diameter, remapped the distribution to a new size grid, and adjusted the data to standard conditions (273.15 K, 101 325 Pa).

Further information on the removal of artefacts can be found in Sect. S2 in the Supplement. In addition, a comparison between the particle concentrations measured by NAIS and the DMPS system can be found in Sect. S2.5; we report a significant overestimation of particle number concentrations as measured by the NAIS in comparison to the DMPS system, particularly at the smallest diameters (see Figs. S9–S11). It should be noted that the particle number size distributions presented in this study represent that of dry aerosol particle sizes. The measured particle size distributions for

both the NAIS and DMPS were not corrected for hygroscopic growth and thus do not reflect ambient conditions.

When assessing the qualitative and quantitative nature of NPF events, it is important to distinguish between the production of newly formed particles ($\sim$ 2–4 nm) on the one hand and subsequent particle growth on the other. To qualify as an event, not only does formation of ultrafine particles need to be present, but also the subsequent growth of the particles. Growth can last for several hours and in some cases multiple days, with the latter timescale suggesting that the NPF events occur on a regional scale (Kecorius et al., 2019; Ström et al., 2009). In this study, we distinguish between (1) *on-site formation*, defined as occasions when the concentration of 2–4 nm particles clearly rises above the background level, and (2) *formation and subsequent growth*, defined as a combination of *on-site formation* followed by subsequent growth. The latter is identified by visual inspection of the behaviour of the growing nucleation mode during the time it is present until when it disappears.

2.3.1 NPF classification

New particle formation events were classified using schemes described by Dal Maso et al. (2005) and Aliaga et al. (2023). The classification schemes are used complementary. The classification by Dal Maso et al. (2005) focuses more on formation and growth and is perhaps more intuitive to understand; however, it struggles with a large number of undefined cases. On the other hand, the nano-ranking analysis developed by Aliaga et al. (2023) can be used to explore the NPF intensity and focuses on the formation of nucleation mode particles as opposed to the subsequent growth. The Aliaga method classifies NPF events into three groups based on the overall ranking of NPF intensity, avoiding the problem with unidentified event days (see Fig. S16 for the groups). The two classification methods can be compared with one another (see Fig. S14). We used the method for the intensity parameter and the diameter range that showed the best comparison with Dal Maso et al. (2005), i.e. the daily maximum for the total number concentration of 2.8 nm and 5 nm particles ($\Delta N_{\mathrm{max},2.8-5}$).

Dal Maso classification system

In the Dal Maso et al. (2005) scheme an NPF event is defined if there exists a nucleation mode (3–25 nm) which prevails for several hours and shows signs of growth; these events are further subdivided into three separate classes, namely, Class Ia and Ib and Class II. Class I and Class II events are separated on the basis of whether the growth and formation rates of the well-behaved size distribution can be determined with good confidence. Class I is further divided into Class Ia and Class Ib depending on whether there are pre-existing particles obscuring the newly formed mode (Dal Maso et al., 2005). Undefined events are days where there are sporadic occurrences of nucleation mode particles, and this classification is used to separate clear events from clear non-events. For examples of the different classifications and their respective averages see Figs. S12 and S13, respectively.

In this study, undefined days include days where the occurrence of nucleation mode particles (3–25 nm) is linked to windblown snow and situations when ZEP is enveloped by clouds. For more details regarding these sampling conditions see Sect. S2.1 and S2.2 for in-cloud sampling and windblown snow events, respectively. As a result, days classified as undefined are ones which experience bursts of nucleation mode particles, either from windblown snow (see Fig. S4), in-cloud conditions (see Fig. S2), non-growing NPF, or a combination of all three. There is a definite increase in the concentration of particles with diameters around 5 nm when the NAIS measures in conditions of low visibility, and this is not observed in other instruments (see Fig. S3). For windblown snow events, particles with diameters less than 20 nm observed considerable increases in concentrations when the wind speed passed roughly 10 m s^{-1} (see Fig. S5). Non-events are days that display no nucleation mode (3–25 nm). It is important to note that this scheme assumes that particle formation occurs over a geographically wide area more or less simultaneously. Identification and classification were performed using daily surface plots of particle number size distribution based solely on NAIS data, that is, 2.5–40 nm.

It should be noted that there is a degree of subjectivity to this classification approach as to what is considered a certain class. The addition of the NAIS, in combination with the DMPS system, made it easier to detect events using surface plots, especially when the growing mode struggled to surpass $\sim$ 6 nm. However, we were not able to identify any NPF events with the NAIS that we could not identify with the DMPS system, as close inspection of the number concentration of the lowest size bins of the DMPS system was sufficient to recognise NPF events.

Nanoparticle ranking analysis

The nanoparticle ranking analysis method developed by Aliaga et al. (2023) provides a more continuous method to characterise atmospheric NPF, allowing users to gauge the strength of NPF. The nanoparticle ranking analysis was utilised using the daily maximum concentration of 2.8–5 nm particles ($\Delta N_{\mathrm{max},2.8-5}$), from the negative channel of the NAIS, as the intensity parameter (note that no background value was used, unlike in Aliaga et al., 2023, due to the low concentrations measured at ZEP). In this study, periods which experienced windblown snow or in-cloud events were removed before applying the nanoparticle ranking method (see Figs. S7 and S8), as opposed to the Dal Maso et al. (2005), approach which classified them as undefined days. Special care was taken to clean the data before utilising the nanoparticle ranking analysis method; however, it may still be the case that not all in-cloud and windblown snow events

were removed successfully (see Sect. S2.1 and S2.2). Wind-blown and in-cloud events can influence the daily maximum without necessarily reflecting NPF activity. The strength of NPF activity was split into three groups depending on the intensity (i.e. *g1*, *g2*, *g3*), where *g3* is the most intense event, followed by *g2* and then *g1*; see Aliaga et al. (2023) for more details (see Figs. S15 and S16).

2.3.2 Growth rates

The growth rate (GR) describes the rate of change of the modal diameter during an NPF event. For the GR estimation, NAIS and DMPS size distributions were merged at the maximum diameter of the NAIS size range (i.e. 40 nm). The NAIS and DMPS data were both interpolated to 15 min arithmetic means using linear interpolation. The start and end of each NPF event including their sequential growth (i.e. *formation and subsequent growth*) were estimated by visual inspection. The growing nucleation mode was isolated, and the GR was estimated for the full duration of the NPF event (see Fig. S17). For each size bin, we applied a Gaussian filter (sigma = 1) and found the time in which the concentration of a particular size bin experienced the highest maximum rate of change. Essentially, the evolution of the nucleation mode was tracked using the timings for each identified peak in the rate of change of the growing nucleation mode diameter. The GR was calculated using a simple linear ordinary least squares (OLS) method.

It should be noted that the aforementioned issues concerning the overestimation of particle number concentrations for the NAIS measurements do not impact the calculation of GR as it only examines the changes to the diameter of the nucleation mode. Very few events grew beyond the limit of the NAIS (i.e. 40 nm); hence the impact of a diameter jump from NAIS to DMPS was not considered. We tried to measure the GR of all NPF events (e.g. Class 1a, 1b, and II), even though by definition Class II events lack the strength and consistency, making it difficult to calculate GRs (Dal Maso et al., 2005). The GRs for some Class II events were not estimated due to uncertain tracking of the nucleation growth.

2.3.3 Particle formation rates

The formation rates, namely J_{3-7}, J_{7-25}, and J_{3-25} ($\mathrm{cm^{-3}\,s^{-1}}$), were estimated using the following equation:

$$J_{i-j} = \frac{\mathrm{d}N_{i-j}}{\mathrm{d}t} + \mathrm{Coag} \times N_{i-j} + \frac{\mathrm{GR}}{\Delta d_p} \times N_{i-j}, \quad (1)$$

where J_{i-j} is the formation rate of particles between diameters i–j nm, CoagS is the coagulation sink of the pre-existing particle population, GR is the growth rate between i and j nm, $\Delta \mathrm{d}p$ is the difference in diameter between i and j in nanometres, and N_{i-j} is the total concentration of particles between i and j nm (Fig. S18 represents an example for calculating formation rates for particles between 3 and 7 nm).

The Python GUI, *npf-event-analyser*, was used to provide additional complementary estimations of the GRs and formation rates for the NPF events (i.e. in addition to the OLS fitting method). When using the *npf-event-analyser* the max concentration method was used for the estimations of GR and J.

2.3.4 Condensation sink

The condensation sink (CS) is defined as the rate at which non-volatile vapours condense onto pre-existing particles (Kulmala et al., 2012). The twin DMPS system (5–850 nm) was used to calculate CS for SA vapour. The method for the determination of CS is described by Dal Maso et al. (2002) and uses the following equation:

$$\mathrm{CS} = 2\pi D \int_{i}^{d_{p,i\max}} d_{p,i}\,\beta\left(d_{p,i}\right) N\left(d_{p,i}\right) \mathrm{d}d_{p,i}, \quad (2)$$

where $d_{p,i}$ is the diameter of a particle in size class i, N_i is the particle number concentration in the respective size class, and D is the diffusion coefficient of the condensing vapour (in this case condensing vapours were assumed to have H_2SO_4 diffusion properties). We used the transition regime correction factor β from Fuchs and Sutugin (1970).

2.3.5 Concentration of condensable vapours and source strength

The concentration of vapours (C_v) required to sustain the calculated GRs and their respective source rates (Q) were estimated using the following equation and assuming the condensation of H_2SO_4:

$$C_\mathrm{v} = A \times \mathrm{d}D_p/\mathrm{d}t, \quad (3)$$

where A is the constant $1.37 \times 10^{-7}\,\mathrm{h\,cm^{-3}\,nm^{-1}}$ representative of the molecular properties of SA, and $\mathrm{d}D_p/\mathrm{d}t$ is the rate of change of the nucleation mode, i.e. GR from the start of the NPF until it stops growing (see Sect. 3.1.5 below and Dal Maso et al., 2005, for further details). The constant A incorporates the probability that sulfuric acid molecules will "stick" to particles upon collision, the change in volume which occurs after collision and condensation, and also the frequency of collisions (Fiedler et al., 2005).

2.4 Air mass analysis

2.4.1 Transport model

Air mass back trajectory analysis was performed using the Hybrid Single-Particle Lagrangian Integrated Trajectory model (HYSPLIT V5.2.1) (Draxler and Hess, 1998; Stein et al., 2015). Ensemble back trajectories were initialised every hour starting at the latitude and longitude of ZEP and at a

height of 250 m above ground level (a.g.l.). The ensemble was generated by offsetting the meteorological grid point by one in the horizontal (i.e. dxf = 1.0, dyf = 1.0) and by the default offset of 0.01 sigma units in the vertical (∼ 250 m), thus generating 27 back trajectories for all possible offsets in X, Y, and Z. The starting height of 250 m ensured that the starting location of all the ensemble members was at the surface or above. The back trajectories were calculated for 5 d back in time. Global Data Assimilation System (GDAS) 1° × 1° archive data (http://ready.arl.noaa.gov/archives.php, last access: 8 August 2024) were used as the meteorological fields. No averaging of the back trajectories was performed, reducing them to single back trajectories. HYSPLIT was run from the desktop using the Python package *pysplit* (https://github.com/mscross/pysplit, last access: 13 April 2021).

The accumulated solar flux in the most recent 6 h prior to arrival was used for the solar insolation term used throughout this study. The solar flux was taken from the original GDAS-derived HYSPLIT output. Furthermore, only endpoints within the mixed layer were used as this is when air masses are influenced by the surface. The last 6 h were used, as opposed to a longer duration, to place more significance on solar radiation closer to the receptor; an accumulated solar flux consisting for a longer duration could lead to misleading results.

2.4.2 Chlorophyll *a* data

Daily mapped chlorophyll *a* data derived from satellite observations (Aqua MODIS) (downloaded from https://oceancolor.gsfc.nasa.gov/l3/, last access: 4 October 2024) were utilised along with the HYSPLIT output to estimate the chlorophyll *a* exposure. Exposure of the air masses to chlorophyll *a* was calculated based on the equation developed by Park et al. (2018), which linked chlorophyll *a* with DMS measurements on site at ZEP. Chlorophyll *a* exposure was essentially used as a proxy for DMS emissions. DMS in turn can form H_2SO_4 via SO_2, although this was not explicitly addressed by Park et al. (2018). It should be noted that DMS is not only a precursor to H_2SO_4, but also MSA. Park et al. (2018) utilised the relationship between DMS and air mass exposure to chlorophyll *a* to account for the differences in the species-specific phytoplankton population between the Greenland Sea and the Barents Sea. For more details on the calculation of the chlorophyll exposure see Sect. 12.

2.4.3 Nucleation site estimation

The method utilised here is similar to the NanoMap analysis developed by Kristensson et al. (2014) in which the geographic position of where new particle formation took place was estimated based on the particle number size distribution measurements during NPF events and HYSPLIT back trajectories. In this study, the duration of the nucleation mode was calculated. For every hour of the NPF event, back trajectories were initialised. The length at which the back trajectories were initialised depended on how long the event had lasted. In short, i hours after the event began, the back trajectory will have been initialised to run i hours backwards. So, for every hour except the start time the back trajectories were initialised for the following length of time: $\textit{back trajectory length} = \textit{duration} - (\textit{end time} - t)$, where $t \in$ (end to start times). Hence, for an NPF event that lasts 7 h, six back trajectory ensembles were calculated for varying lengths from 7 to 1 h long.

2.4.4 Air mass marine regions

The endpoints for every 5 d back trajectory ensemble were assigned to a marine region, e.g. the Arctic Ocean, Greenland Sea, Barents Sea, Norwegian Sea, or North Atlantic Ocean (see Fig. S21 for defined regions). Days were assigned to a specific marine region based on the cumulative residence time in the specific sector. A threshold of 0.5 (50 %) was used as a qualifier. Days without clear source preference, i.e. the air masses that did not reach the 50 % threshold for either of the pre-defined source regions, were classified as mixed.

3 Results and discussion

3.1 Seasonality and interannual variability

3.1.1 Annual cycle of NPF events

The 848 d of valid NAIS measurements (17 April 2022 to 4 October 2024) are classified according to the Dal Maso et al. (2005) classification system. A total of 157 d are classified as NPF events, either Class Ia events (28), Class Ib (19), or Class II (110). A total of 438 d are classified as undefined, and the remaining 271 d are considered to be either non-event days (253) or consisting of too few data (i.e. defined as < 12 h of data per day) (18) (see Fig. 1). Overall, this meant that 19 % of days with valid NAIS measurements experienced an NPF event (i.e. Class Ia, Ib, or II). The majority of days (52 %) are classified as undefined due to the appearance of a non-growing nucleation mode that persisted for some hours. The undefined days are further sub-divided into those containing windblown snow events (19 % of all data) and in-cloud events (8 % of all data) (see Fig. S6). Of the 438 undefined days, 72 are a result of non-growing bursts (i.e. 17 % of the undefined days).

The monthly frequency of NPF events (i.e. Class Ia, Ib, or II) shows events first appearing in April (see Fig. 1), reaching a peak, in terms of the occurrences per month, in May to July with approximately 30 %–40 % of days experiencing NPF. The daily occurrence decreases during the month of June compared with the preceding and succeeding months, a consistent finding throughout the 3 years of data. After July, the frequency of events declines towards the end of summer

and into autumn, where NPF events cease to be present beyond November. NPF events were observed as late in the year as November, which is interesting given that this is during the polar night, when the sun stays below the horizon (as witnessed by ZEP), and thus ZEP experiences negligible solar radiation. Multiple NPF events were observed during the polar-night period (see Sect. 3.1.3 for more details). April 2022 appeared anomalous perhaps given that the measurements for that month were not an entire month as the measurements started on 17 April 2022.

Prior studies at ZEP, which used slightly different event classification schemes, reported the occurrence of NPF events to be within the range of 18 %–23 % (Dallósto et al., 2017; Heintzenberg and Leck, 2012; Lee et al., 2020). Nieminen et al. (2018) reported NPF day frequencies of 14 % (March–May), 34 % (June–August), 6.6 % (September–November), and 0 % (December–February). Lee et al. (2020) observed the highest frequency in terms of the formation and growth of N_{3-25} particles in June (> 40 %), with the NPF frequency in May and July being ~ 40 % and < 40 %. Dome C in Antarctica and Alert in Greenland are two other polar sites with annual NPF frequencies between 10 % and 20 % (Nieminen et al., 2018), comparable to ZEP.

3.1.2 Interannual variability in NPF intensity, solar insolation, DMS, and CS

The interannual variability in the following main parameters, namely NPF intensity, solar insolation, DMS concentration and the CS, is explored in Fig. 2a–b. A proxy for the intensity of events, as opposed to the frequency, was determined by utilising elements of the nanoparticle ranking analysis developed by Aliaga et al. (2023). The maximum daily concentration in 2.8–5 nm particles ($\Delta N_{\max,2.8-5}$) was used to represent the strength of NPF activity (shown to correlate well with calculated J), i.e. the NPF intensity. See Sect. 2.4.1 in the Methods for more details concerning the nanoranking method and about the definition of solar insolation.

$\Delta N_{\max,2.8-5}$ shows various peaks throughout the annual cycle; however, the one striking feature is that every year $\Delta N_{\max,2.8-5}$ has its first and highest peak occurring in late spring and the beginning of summer (i.e. end of April in 2022, beginning of June in 2023, and towards the end of May in 2024) (see the red curve in Fig. 2a). In terms of the annual cycle in NPF event frequency (see Fig. 1), the first peak in NPF event occurrences matches the April–June peak in increased $\Delta N_{\max,2.8-5}$ (Fig. 2a). However, the succeeding peak in NPF event frequency (i.e. in July in Fig. 1) coincides with reduced intensity ($\Delta N_{\max,2.8-5}$). The seasonality of the $\Delta N_{\max,2.8-5}$ value follows that of the solar insolation, and for the years 2023 and 2024, the maximum NPF strength/intensity (i.e. $\Delta N_{\max,2.8-5}$) coincides with the greatest mean solar insolation; a much better relationship is observed when selecting for air masses within the mixed layer as this is when arriving air masses are influenced by the surface (i.e. the orange bars in Fig. 2a). Averaging the intensity parameter and correlating it to the solar insolation calculated based on the entire air mass and the parts within the mixed layer (ML) shows that selection of air masses within the ML leads to a better correlation (see Fig. S27). The annual cycle for the calculated CS exhibits a sustained maximum in late winter and early spring due to the Arctic haze (i.e. February–May), and the CS stays high into the summer before reaching a minimum in autumn, typically the cleanest part of the year (Tunved et al., 2013) (see Fig. 2b). During the Arctic haze period, long-range-transported air masses from Eurasia bring aged aerosol, leading to the higher CS. At the same time, this period is characterised by higher sulfate and SO_2 concentrations, mainly of anthropogenic origin (Platt et al., 2022), and hence there are NPF events occurring and high increased NPF intensity. One additional aspect is that it is clear that increases in $\Delta N_{\max,2.8-5}$ occur during periods where there was a slight decrease in CS, below that of the seasonal CS average. For example, the peak in $\Delta N_{\max,2.8-5}$ in April in 2022 (see Fig. 2b), which occurs slightly prior to the maximum solar insolation, can potentially be explained by the reduction in the CS during that period.

The solar intensity is a controlling factor in the production of SA (i.e. H_2SO_4) via the oxidation of SO_2. In the Arctic, DMS acts as a significant source of sulfate; however, other sulfur compounds can be oxidised, e.g. carbon disulfide and hydrogen sulfide (Pei et al., 2021). The coagulation sink (CoagS) acts as a sink for the newly formed particles, and the CS acts as a sink for nucleating vapours; thus high CoagS and CS can inhibit NPF. NPF days with greater intensity (i.e. $\Delta N_{\max,2.8-5}$) are skewed towards the end of spring and beginning of summer. Similarly, solar insolation is also shifted towards the start of summer, even though the theoretical solar maximum has a symmetrical distribution centred around the middle of summer (see red shaded region in Fig. 2a). The skewed pattern in both the solar insolation and NPF intensity ($\Delta N_{\max,2.8-5}$) can perhaps be explained by annual changes in cloud cover (see Maturilli and Ebell, 2018, for the frequency occurrence of cloudy sky, increasing to ~ 80 % during the summer from an April minimum of ~ 40 %–60 %). Late autumn experiences numerous, but relatively weaker, NPF events, with peaks in $\Delta N_{\max,2.8-5}$ (~ 100–$500\,\mathrm{cm}^{-3}$) every year at the end of the summer despite the relatively small solar insolation. The transition period between summer and haze (i.e. October–January) is typically the cleanest part of the year and thus exhibits the lowest CS (Tunved et al., 2013). During this part of the year the small amount of solar insolation and vapours present are enough to trigger NPF, possibly as a result of the low CS.

Finally, DMS is the main source of sulfur for clean marine aerosol particles and constitutes an important compound in regards to NPF via its oxidation products. Numerous peaks in DMS are observed during the summertime, with a maximum observed in July (see Fig. 2b). Elevated concentrations of DMS at ZEP coincide with air masses which traverse over

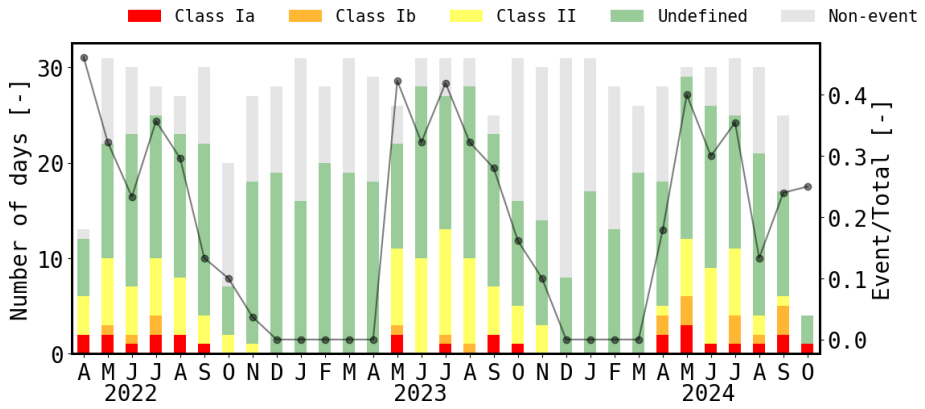

Figure 1. Number of days per month classified as either Class Ia (red), Class Ib (orange), Class II (yellow), undefined (green), or non-event (grey). The left-hand axis is the number of days classified based on the total number of valid measurement days (i.e. total). The right-hand side is the fraction of events (i.e. Class Ia, Ib, and II) over the total number of valid measurement days (i.e. Class Ia, Class Ib, Class II, undefined, and non-event). The fraction is given by event/total. Almost 3 years of Neutral cluster and Air Ion Spectrometer (NAIS) particle number size distribution data is classified using the Dal Maso et al. (2005) classification system.

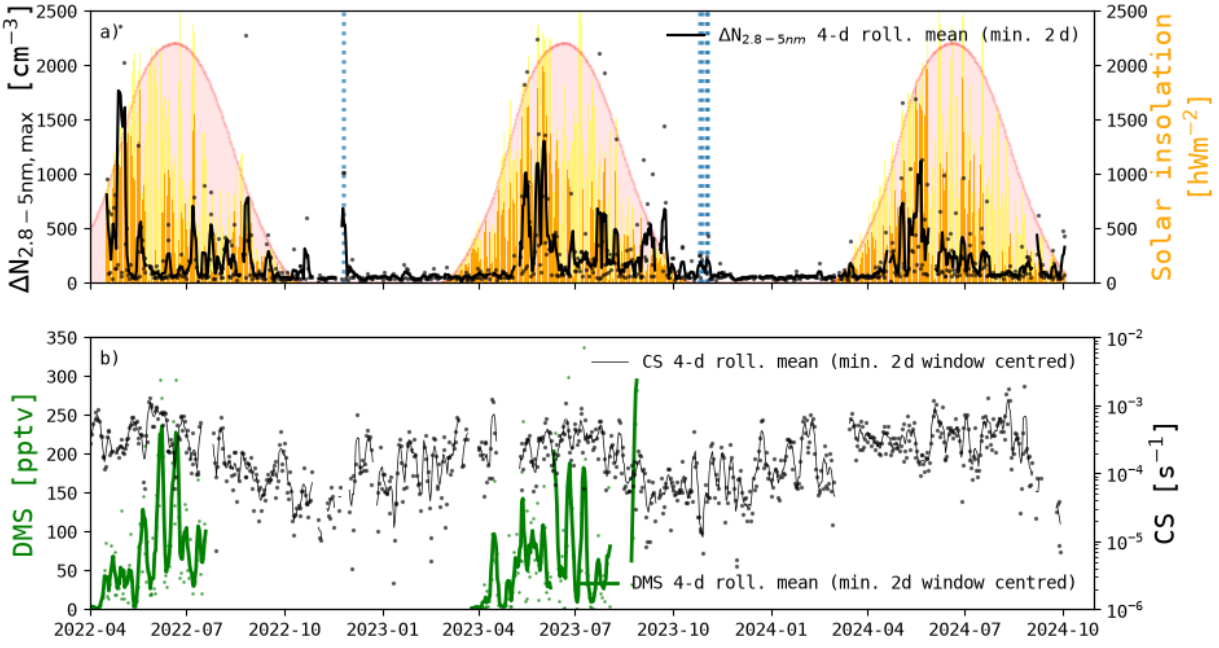

Figure 2. Time series of **(a)** the NPF intensity parameter ($\Delta N_{\mathrm{max},2.8-5}$; black dots), defined as the daily maximum particle number concentration between 2.8 and 5 nm. The black line shows the centred 4 d running mean. Orange bars indicate daily solar insolation accumulated over the preceding 6 h for air masses arriving at ZEP within the mixed layer (Sect. 2.4.1); faint yellow bars show the same for all air masses. The red shaded region is there for comparison to the yellow and orange bars and represents 6 times the average hourly clear-sky global horizontal irradiance (GHI) at ZEP. **(b)** Valid DMS measurements (green) and the condensation sink (CS; black dots, daily means) with its centred 4 d running mean (black line). Dashed blue lines indicate polar-night periods.

marine regions containing chlorophyll *a* (see Figs. S30–S37, but also noted by Park et al., 2018).

3.1.3 Events with minimal solar insolation (i.e. polar-night events)

Contrary to expectations, during the polar night (i.e. when the sun does not cross the horizon at Ny-Ålesund) a number of NPF events are observed. As shown earlier, solar insolation is clearly one of the driving parameters for NPF occurrence and intensity, and Ny-Ålesund in November does not receive any direct solar radiation (see Fig. S19 for examples of the polar-night events). For the November polar-night events, air mass back trajectories indicate that air masses have to travel at least half a day backwards before reaching Ny-Ålesund to

experience direct solar radiation. In total, five of these events are observed and are detailed in Table 1.

The polar-night NPF event starting on 25 October 2023 appears to be a transported event (TE; see Dada et al., 2018, for details on the definition of a transported event) as we do not observe the entire growth of freshly nucleated particles; instead the growing nucleation mode begins at 4 nm. The extremely low accumulated solar radiation experienced by the arriving air masses during these events means that there should be little available nucleating vapours (less oxidation before reaching ZEP). Two other Arctic sites, namely Utqiaġvik, Alaska, and Tiksi, Russia, also observe NPF events without the sites experiencing any solar radiation (Asmi et al., 2016; Kolesar et al., 2017). However, at these two sites the suggestion is that anthropogenic emissions of semi-volatile gases from nearby oil fields or the build-up of anthropogenic emissions during the haze period can explain these events, an interpretation which is not applicable for ZEP.

The vertical component of the arriving back trajectories associated with these polar-night events shows that air masses originated from higher altitudes (Fig. S17) and that these air masses descend before arriving at ZEP. One possible explanation for these types of events could be that precursor gases, originally emitted from the surface, are transported to high altitudes where the CS is sufficiently low enough to allow them to survive long enough to be nucleated on descent to ZEP. The air masses travel further south and higher in altitude, where the small amount of solar radiation potentially allows for photochemical production of nucleating vapours to build up.

3.1.4 Start times and duration throughout the year

The median duration of NPF events, including their subsequent growth, is approximately ~ 10 h and seems to be fairly consistent across the annual cycle, with a decrease towards the autumn (see Fig. 3a). Of all events, $75\,\% > 7$ h, and $90\,\% > 4$ h. During the sunlit period, the starting time of events is typically around 09:00 (UTC) for the period April to August. From September onwards, the onset of the observed NPF shifts to later in the day (Fig. 3b). For the period August to October, onset of NPF is approximately 8 h after sunrise at Ny-Ålesund (note that the gradient of the two slopes in Fig. 3b remains constant, but the start time is shifted by 8 h). This could reflect that during the NPF season there is a delay of approximately 8 h from the minimum solar intensity to the onset of NPF, and this could be related to the time it takes for precursor gases to accumulate.

Lee et al. (2020) suggested that the duration of NPF at ZEP was approximately 6–7 h, with the longest duration in summer. In addition, NPF start times were 13:00–14:00 (local time, which is 11:00–12:00 UTC in the summer time). The start times observed at ZEP, here in this study, were typically 2 h earlier, perhaps as a result of the slightly lower minimum particle diameter detection and not the same definition of the onset of nucleation.

3.1.5 Seasonality of growth rates and formation rates

The mean (median) GRs for all the events are 2.2 (1.5) $\mathrm{nm\,h^{-1}}$. For Class Ia, Ib, and II events the average GRs are 1.4 (1.0), 1.7 (1.2), and 2.6 (1.2) $\mathrm{nm\,h^{-1}}$, respectively. The largest GRs occur during July: 4.0 (2.1) $\mathrm{nm\,h^{-1}}$. The polar-night events exhibit a significantly reduced GR of 0.43 (0.35) $\mathrm{nm\,h^{-1}}$ (see Fig. 4a). Using the *npf-event-analyser* for the Class Ia events the GRs are 0.9 (1.1), 2.1 (2.6), and 4.1 (4.4) $\mathrm{nm\,h^{-1}}$ for 3–7, 3–25, and 7–25 nm diameter ranges.

The GRs presented here agree well with earlier estimates of GRs by Nieminen et al. (2018) reporting a $\mathrm{GR_{10-25\,nm}}$ at ZEP within the range of 1.2–1.6 $\mathrm{nm\,h^{-1}}$. Kerminen et al. (2018) report a median GR for the Arctic of 2.3 (0.23–4.1, 5th and 95th percentiles) $\mathrm{nm\,h^{-1}}$, the site type (i.e. compared with other geographical regions) with the smallest GRs.

Formation rates for $J_{3-7\,\mathrm{nm}}$ are $0.14 \pm 0.23\,\mathrm{cm^{-3}\,s^{-1}}$ (mean $\pm$ SD) for all events in which calculations of J and GR could be ascertained (see Fig. 4b for the seasonality). Formation rates are generally greater in May, with 2023 not exhibiting this maximum in May. The formation rates for $J_{3-7\,\mathrm{nm}}$, $J_{3-25\,\mathrm{nm}}$, and $J_{7-25\,\mathrm{nm}}$ are estimated to be 0.28 ± 0.33, 0.40 ± 0.35, and $0.31 \pm 0.28\,\mathrm{cm^{-3}\,s^{-1}}$ (mean $\pm$ SD) for Class Ia events (using the max concentration method and *npf-event-analyser*; see Sect. 2.3.3 in the Methods).

Previous studies also estimate J for various diameters at Ny-Ålesund and ZEP. Beck et al. (2021) reports a $J_{1.5}$ equal to $0.27\,\mathrm{cm^{-3}\,s^{-1}}$ (Beck et al., 2021). Nieminen et al. (2018) presents the seasonal medians for J_{nuc} of nucleation mode particles (10–25 nm) varying from $0.08\,\mathrm{cm^{-3}s^{-1}}$ in spring to $0.032\,\mathrm{cm^{-3}\,s^{-1}}$ in summer and to $0.0066\,\mathrm{cm^{-3}\,s^{-1}}$ in autumn. Lee et al. (2020) give J_{3-7}, J_{7-25}, and J_{3-25} values ranging between 0.001–0.54, 0.003–0.5, and 0.007–$0.61\,\mathrm{cm^{-3}\,s^{-1}}$, respectively, and the averages for J_{3-7}, J_{7-25}, and J_{3-25} are 0.04, 0.09, and $0.12\,\mathrm{cm^{-3}\,s^{-1}}$. Kerminen et al. (2018) report a median Arctic J (i.e. varying size ranges) of $0.51\,\mathrm{cm^{-3}\,s^{-1}}$.

In comparison to GRs and Js at other sites (e.g. Kerminen et al., 2018; Nieminen et al., 2018), we see that processes within the Arctic, as observed at ZEP, are significantly slower. In urban environments, compared with more remote ones, estimations for J are significantly larger due to the larger coagulation sink that needs to be overcome (Cai and Jiang, 2017); here, the coagulation sink is much lower than in urban environments.

3.1.6 Seasonality of condensable vapours

The concentration of condensable vapours (C_{v}) required to sustain the GRs is estimated using Eq. (3) and the calculated growth rates for the various classes of events (i.e. Class Ia,

Table 1. Polar-night event observation from 17 April 2022 to 4 October 2024. All times are expressed in coordinated universal time (UTC).

Polar-night day	Date/time	Duration [h]	GR [nm h^{-1}]
1.	25 November 2022, 20:00, to 26 November 2022, 15:00	15	0.38
2.	25 October 2023, 20:00, to 26 October 2023, 23:50	23	0.41
3.	a. 28 October 2023, 01:00, to 29 October 2023, 02:00 b. 28 October 2023, 12:00, to 29 October 2023, 15:00	25 27	0.17 0.27
4.	1 November 2023, 09:00, to 2 November 2023, 18:00	28	0.32
5.	2 November 2023, 21:00, to 3 November 2023, 06:00	8	0.78

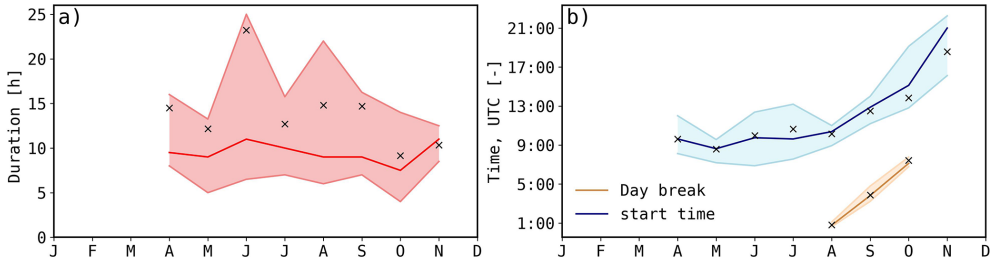

Figure 3. **(a)** Duration of the entire growth of newly formed particles from the first measurable size bin, i.e. 2.5 nm, to the largest size bin. **(b)** Average start time of the observed new particle formation (NPF) event. Monthly means displayed by crosses and medians by the red and blue lines, respectively, along with a shaded region representing the 25th and 75th percentiles. Time when the global horizontal irradiance (GHI) is greater than zero (i.e. daybreak) is displayed in orange. The average daybreak time for the months April until July is not applicable, since the sun is constantly above the horizon (as experienced by ZEP during the polar day). Time is given in terms of coordinated universal time (UTC). Note that a day break value for November to March is not applicable as these experience the polar night.

Ib, and II). We show that C_v increases until July before decreasing during the autumn and into the winter months. It is striking to note that the seasonal variation is similar to that of the sum of the measured concentrations of potential aerosol precursor gases measured in Ny-Ålesund during a 2017 campaign (see Fig. 5). The estimated C_v is also of a similar magnitude to the combined sum of measured HOMs, sulfuric acid (H_2SO_4), methanesulfonic acid (MSA), and iodic acid (HIO_3). For Ny-Ålesund, Beck et al. (2021) report increasing IA, SA, and MSA concentrations from the start of the sunlight period and high concentrations prevailing before decreasing around mid-June. HOM concentrations averaged around $\sim 1.8 \times 10^6$ cm^{-3} during the spring before increasing to 2.3×10^6 cm^{-3} in June. As a ratio of the total available precursor vapours HOMs account for approximately 0.78 of the entire concentration of precursor vapours after June, and prior to June this fraction was approximately 0.24 (see Fig. S24). It can therefore be argued that the composition of condensable vapours undergoes a dramatic transformation around the start of June, and the composition of newly formed particles during the initial spring peak is different to that of the subsequent peaks after June (see Figs. 1 and 2). Boyer et al. (2024) measured the concentrations of condensable vapours in the Arctic, however at higher latitudes (> 80° N). The estimated C_v at ZEP was on average 5.9 times greater than the combined concentrations of the measured precursor gases given in Boyer et al. (2024) (see Fig. S23). At higher latitudes (> 80° N), there is potentially less photochemistry and biological activity; moreover, the potential sources of precursor gases are more limited (Brean et al., 2023) and may be more influenced by the sea ice cover, further reducing the availability of precursor gases and giving rise to the difference between the estimated C_v at ZEP and total concentrations during MOSiAC.

3.2 Positive and negative ions during NPF

The polarity of air ions, which aid in nucleation, provides information about the composition of the newly formed aerosol particles. Cluster air ions are typically defined between 0.8 and 1.7 nm, whilst intermediate ions range from 1.6–7.4 nm. Intermediate ions are created in the initial stage of nucleation and are typically formed when neutral nanoparticles encounter cluster ions and acquire their charge (Tammet et al., 2014). Negative ions can be linked to IA and SA, to name a couple of compounds. Unfortunately, due to an instrumental problem related to a consistent loss of the negative cluster ions experienced during the measurement campaign (see Sect. S2.6) it was not possible to measure the concentration of negative ions less than 2 nm.

The total number of positive ($N^+_{2-4\,nm}$) and negative ($N^-_{2-4\,nm}$) small intermediate ions (2–4 nm) within the grow-

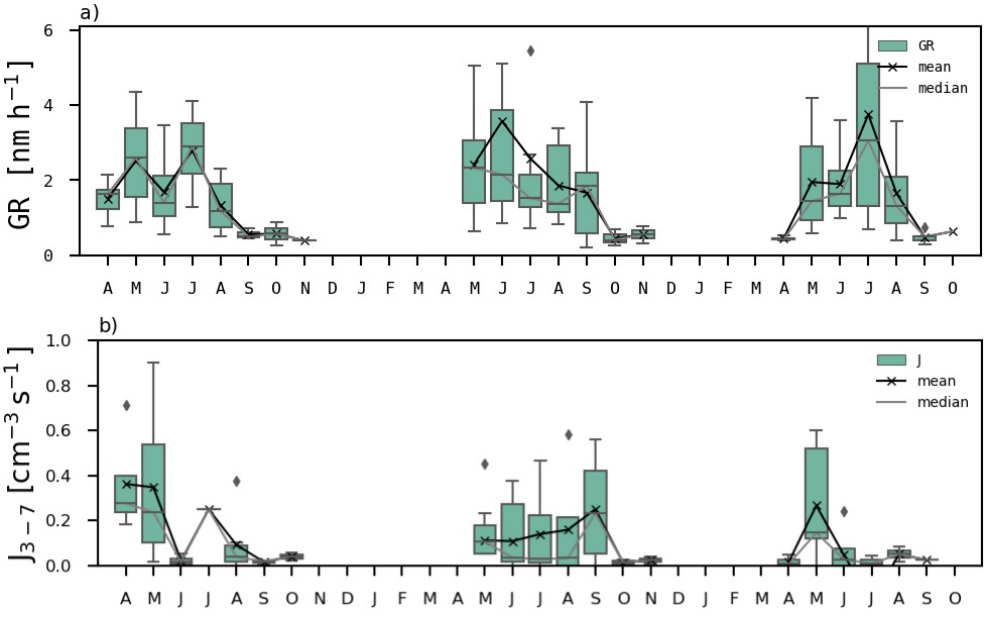

Figure 4. **(a)** The calculated growth rates (GRs) and **(b)** calculated median formation rates for particles between 3 and 7 nm (J_{3-7}) throughout the measurement period are represented by box whiskers, which display the monthly growth rate averages and include the median and 25th–75th percentiles. The green box whiskers refer to the average GRs/J_{3-7}s from the start of the NPF until it stops growing. The black line with crosses represents the mean, and the grey lines join the median values. Diamonds represent outliers.

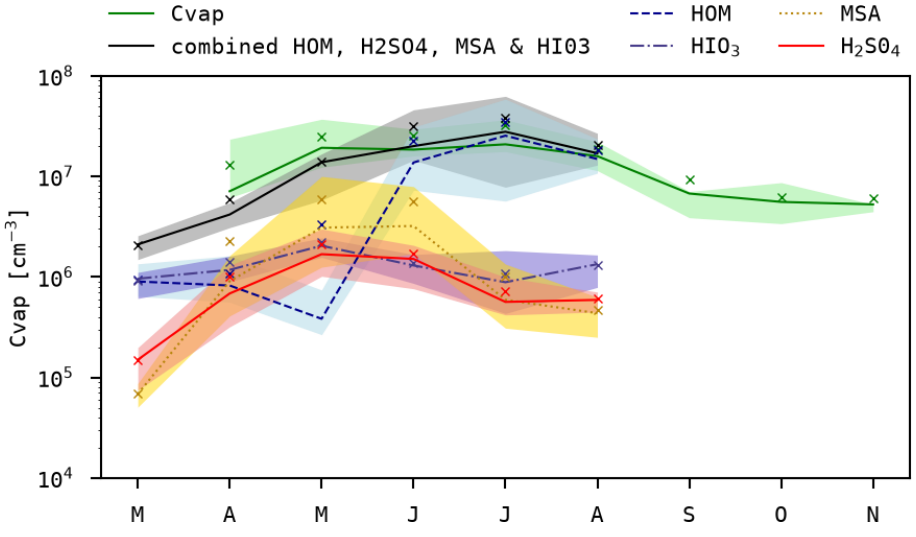

Figure 5. Estimated concentration of condensable vapours (C_v; solid green) compared with measured concentrations: the monthly means (crosses) and medians (thick line), along with the 25th and 75th percentiles (shaded region) for both C_v and Ny-Ålesund measurements. Arctic precursor vapours, namely sulfuric acid (H_2SO_4; solid red), methanesulfonic acid (MSA; dotted gold), highly oxygenated molecules (HOMs; dashed dark blue), and iodic acid (HIO_3; dash dot purple), as well as combined values (grey) from Beck et al. (2021), are displayed. The estimated C_v measurements cover the years 2022 to 2024, whilst the Svalbard measurements from Beck et al. (2021) cover the period 22 March to 23 August 2017.

ing mode are calculated for each NPF event. In May, at the start of the NPF season, we observe the smallest fraction of positive small intermediate ions compared to the total number of small intermediate ions (i.e. the mean and median ratio, $N^{+}_{2-4\,\mathrm{nm}} / (N^{-}_{2-4\,\mathrm{nm}} + N^{+}_{2-4\,\mathrm{nm}})$, ≈ 0.2). The low $N^{+}_{2-4\,\mathrm{nm}}$ / total ratio in May perhaps relates to negatively charged molecules dominating the initial stages of ion-induced nucleation (i.e. compared with positive ions). Moreover, the low ratio in May could be related to the greater NPF intensity (i.e. larger production of negative nucleation mode

particles in May). However, towards the end of the NPF season (i.e. September–November) there is a shift towards a growing nucleation mode (e.g. 2–4 nm) more dominated by positive small intermediate ions, as opposed to negative small intermediate ions (see Fig. 6). The tendency for small intermediate ions (2–4 nm) to exhibit a positive charge appears from September onwards, which is also when there begins to be limited solar insolation and the occurrence of polar-night events (i.e. late October and November); it is also, and perhaps more importantly, when the composition of condensable vapours changes to being dominated by HOMs (see Sect. 3.1.6). However, it needs to be noted that there are few events during September and beyond (29 in total). Despite the lack of information about the cluster ions, the shift in the overall charge of the small intermediate ions, from more negative to more positive, potentially hints at a seasonal change in the vapours contributing to the initial formation of critical clusters.

As mentioned above, Beck et al. (2021) reports higher concentrations of precursor gases with low proton affinity (e.g. MSA, SA, HSO_4^-) during the month of May, while highly oxygenated organic molecules (HOMs) display higher concentrations than SA and MSA during April and from June towards September. Beck et al. (2021) suggest that the events in May were likely initiated by negative ion-induced NPF and relate to sulfuric acid and ammonia nucleation.

Ammonia (NH_4^+) is a possible positively charged cluster ion which could play a role in the shift in polarity (Kirkby et al., 2016); however, it needs to be stressed that further work is needed to ascertain the reason for this shift in the polarity. We were unable to compare the overall polarity charges for small intermediate ions with concentrations of NH_4^+. However, the shift from more negative to more positive small intermediate ions seems to coincide with the increase in concentrations of HOMs relative to the total concentration of other condensable vapours as also indicated above (see Fig. S24).

3.3 Source regions and geo-spatial extent

NPF events are assigned to various marine regions using the method described in Sect. 2.4.5. Air masses that traverse over the Arctic Ocean coincide with the highest number of NPF events (57 in total or 37 % of NPF events; see Table 2). A total of 37 % of air masses are classified as originating from the Arctic Ocean, the largest marine region in terms of contribution. The air masses that mainly originate over the Greenland Sea result in 29 NPF events and show the highest probability of an NPF event occurring, with 27 % of the Greenland Sea air masses being linked to an NPF day. Air masses originating over the Arctic Ocean and Barents Sea have a 19 % and 13 % likelihood, respectively.

The analysis is expanded, using the method outlined in Sect. 2.4.4, by estimating the location of the formation of newly formed particles. The most common location for nucleation to occur is off the western coast of Svalbard, i.e. in the Greenland Sea and Arctic Ocean (see Fig. 7). Furthermore, the Greenland Sea, south-west of ZEP, as opposed to the Barents Sea, is home to more nucleation sites. It is also clear that the vast majority of nucleation sites are estimated to occur over the ocean. The estimated nucleation sites are almost all within a 1×10^6 km radius of ZEP, and the vast majority are fairly close to ZEP (see Fig. 7), a finding which can also be inferred from the observation that the majority of events begin growing from 2.5 nm. Furthermore, from the air mass back trajectory analysis, we gather that air masses typically reside between sea level and the altitude of ZEP (i.e. 0–474 m; see Fig. S20). There is little difference between the altitudes of the arriving air masses for the NPF events compared to all days.

DMS emissions are closely linked to phytoplankton dynamics and abundance and typically occur following phytoplankton biomass maxima (Galí and Simõ, 2015). Numerous studies have tried to link chlorophyll *a*, which is used as a proxy for phytoplankton biomass, with DMS emissions to the atmosphere (Jang et al., 2019). Park et al. (2018) note a strong correlation between DMS concentrations measured at ZEP and air masses traversing over the surrounding ocean with high chlorophyll *a*. They find that the relationship between DMS concentrations and air masses likely exposed to high DMS emissions is stronger for air masses traversing over the Greenland Sea compared with the Barents Sea, therefore suggesting that the Greenland Sea has a DMS production capacity 3 times greater than the Barents Sea. By replicating the method detailed in Park et al. (2018), we also find good correlations between chlorophyll *a* exposure and DMS, however, not for all years and not for the years related to this study (i.e. 2022 and 2023). In the study by Park et al. (2018) the years 2010, 2014, and 2015 were included; however, 2022 and 2023 did not yield such strong correlations. We were unable to replicate the findings presented in Park et al. (2018) for the years 2022 and 2023 (see Figs. S30–S37); however, we could replicate the findings for 2010 (see Fig. S30). We can only speculate about the reasons for the interannual variation between the relationship between chlorophyll *a* and DMS. We argue that because of the large spatial and temporal interannual variability, possible geo-spatial changes in the Dimethylsulfoniopropionate (DMSP)-rich phytoplankton species in the neighbouring seas, a wide range of DMS oxidation timescales depending on photochemistry and available solar insolation (Ghahreman et al., 2019) can all potentially influence this relationship. Furthermore, meteorological factors may lead to inaccuracies in HYSPLIT outputs, along with other environmental factors such as sea ice and cloud cover which can affect DMS oxidation and the lifetime of precursor gases, influencing chlorophyll a satellite retrievals. One study which examined the seas around Iceland found differing positive correlations between DMSP and chlorophyll *a* (i.e. dependent on air mass origin) and seemed to suggest that higher

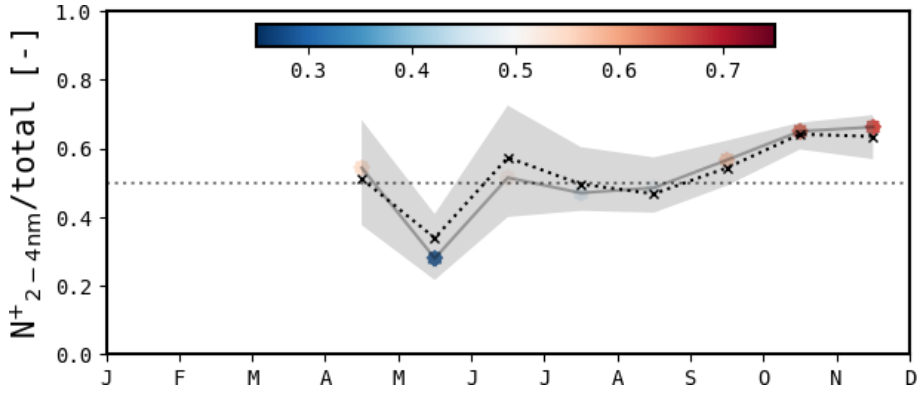

Figure 6. For all new particle formation (NPF) events the monthly ratio of the total number concentration of positively charged small intermediate ions (2–4 nm) over the total concentration of both positively and negatively charged small intermediate ions ($N^{+}_{2-4\,\mathrm{nm}} / N^{-}_{2-4\,\mathrm{nm}} + N^{+}_{2-4\,\mathrm{nm}}$). $N^{-}_{2-4\,\mathrm{nm}}$ and $N^{+}_{2-4\,\mathrm{nm}}$ include only ion concentrations within the identified growing mode between 2 and 4 nm. The mean monthly $N^{+}_{2-4\,\mathrm{nm}}$ / total is presented as a cross, and the median is displayed by coloured circles, blue for an overall negative charge (ratio < 0.5) and red for an overall positive charge (ratio > 0.5). The grey shading displays the 25th–75th percentiles. The dashed black line represents an overall neutral charge of small intermediate ions. It should be noted that there may be some instrumental biases between the two polarities; however, the background concentrations (during no-event periods) display $N^{-}_{2-4\,\mathrm{nm}} / N^{+}_{2-4\,\mathrm{nm}}$ ratios close to unity, ∼ 1.02.

Table 2. The frequency of occurrence of air masses from different sectors compared with the number of events. Both numbers are given in days, followed by a ratio of the two (i.e. likelihood). Although not shown in the table, back trajectories traversed over the Kara Sea on two occasions. The average CS, solar insolation (both mixed-layer and all), maximum daily increase in 2.8–5 nm particles ($\Delta N_{\mathrm{max,2.8-5}}$), and proportion of back trajectory within the mixed layer are given for each marine sector. The averages for these variables are also given during the NPF days and presented in brackets.

Air mass	Region's frequency (days)	Number of NPF events (days)	Likelihood	CS [s^{-1}]	Solar insolation [h W m^{-2}]	$\Delta N_{\mathrm{max,2.8-5}}$ [cm^{-3}]	Proportion in ML
Arctic Ocean	313	57	0.19	0.20 (0.19)	185 (378) 368 (753)	239 (776)	0.63 (0.60)
Greenland Sea	109	29	0.27	0.25 (0.25)	327 (442) 666 (991)	254 (665)	0.60 (0.54)
Barents Sea	69	9	0.13	0.36 (0.29)	118 (211) 597 (1100)	93 (204)	0.32 (0.28)
Norwegian Sea	44	7	0.16	0.25 (0.43)	232 (418) 618 (1330)	136 (382)	0.48 (0.34)
Mixed	303	51	0.17	0.23	184	147	0.54 (0.50)
Total	840	153	0.18	0.23	200	190	0.57 (0.53)

a DMS : chlorophyll-*a* exposure (Echl) ratio is linked to a higher DMPS : chlorophyll *a* ratio (Lee et al., 2023).

The Greenland Sea is connected to a higher likelihood of NPF events; compared with the Barents Sea there is a distinct difference between both seas in terms of the proportion of air masses coinciding with NPF events and the number of nucleation sites estimated to arise from each sea (see Fig. 7). The combined effect of a larger number of air masses coming from the west and an increased NPF likelihood linked to western air masses means that we observe more NPF events off the western edge of Svalbard. This difference could be linked to the finding that the DMS production capacity in the Greenland Sea is estimated to be 3 times greater than that of the Barents Sea, due to more DMSP-containing phytoplankton species (e.g. *Phaeocystis*) (Park et al., 2018). However, another distinct difference between these two source regions is that air masses which traversed over the Greenland Sea experienced more solar insolation and a relatively lower CS average compared to the air masses coming over the Barents Sea (see Table 2). The combination of both high solar insolation and relatively low CS could also explain why NPF likelihood is higher for the Greenland Sea as opposed to Barents

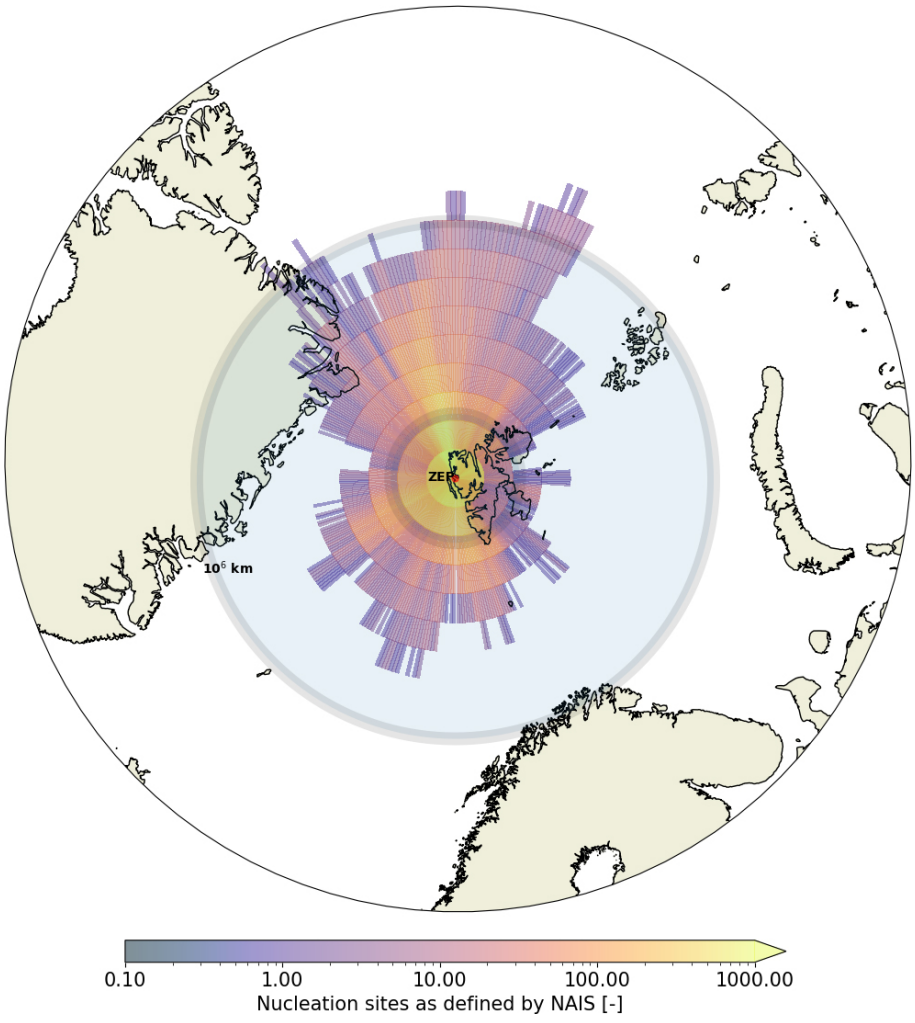

Figure 7. Total number of estimated nucleation sites per grid cell. The unit is based on the number of back trajectories initialised and does not reflect a physical value. Sites of nucleation for Class Ia, Ib, and II events are estimated by using HYSPLIT to trace the likely origin of particles produced during NPF events and initialising the back trajectories based on the duration of the NPF event (see Sect. 2.4.4).

Sea. One further difference is that the Barents Sea has a much larger sea ice coverage compared with the Greenland Sea, and thus there is potentially less open ocean in contact with the lower atmosphere during the NPF season. The reduced availability of DMS given the greater sea ice coverage could additionally help explain the differences in NPF likelihood of the Greenland and Barents seas. The Arctic Ocean is another NPF source region (see Fig. 7 and Table 2). Considering that the Arctic Ocean sector is considerably more covered by sea ice, the NPF precursors are potentially being emitted from sea ice, e.g. iodine and sympagic algae. The Arctic Ocean contributes significantly, in terms of the portion of arriving air masses, between March and May and from September to October (see Fig. S22). HIO_3 and HOMs are both significant contributors prior to May, and HOMs increase in concentration after June.

3.4 Predicting NPF likelihood with condensation sink and solar radiation

In Sect. 3.1.2, we show that NPF events and increases in NPF intensity typically occur during periods of high solar insolation. High solar insolation seems to be a prerequisite for NPF, as it leads to the photochemical production of nucleating compounds. NPF events also seem to require the total surface area of pre-existing aerosol particles (i.e. CS) to decrease below seasonal averages (see Fig. 2). The distribution of solar insolation is statistically significantly different for periods experiencing events as opposed to non-events; for CS it depends on the classification scheme used (as demonstrated using the Mann–Whitney U test; see Fig. S29a–b). NPF events require the concentration of nucleating vapours to exceed a critical concentration, and as the CS acts as a sink of those highly condensable vapours, low CS values promote the potential for nucleation. In this section, we argue that so-

lar insolation and CS can be used as the two central parameters to determine with high certainty the likelihood that a given day will experience an NPF event. For the definition of the term solar insolation refer to Sect. 2.4.1 in the Methods.

The majority of measurements feature the combination of both relatively low solar insolation and low CS ($< 1000\,\mathrm{h\,W\,m^{-2}}$ and $< 0.5 \times 10^{-3}\,\mathrm{s^{-1}}$; see bottom left of Fig. S25b), and on very few occasions there are measurements with a combination of high solar insolation ($> 1000\,\mathrm{h\,W\,m^{-2}}$) and low CS ($< 0.5 \times 10^{-3}$) (see top left of Fig. S25b). Nonetheless, we show that when the combination of high solar insolation ($> 1000\,\mathrm{h\,W\,m^{-2}}$) and relatively low CS ($< 0.5 \times 10^{-3}\,\mathrm{s^{-1}}$; i.e. top left of Fig. S25a and b) arises, an NPF event that day is likely to occur (as defined by Aliaga et al., 2023; see Fig. 8). We find that periods exhibiting high solar insolation ($> 1000\,\mathrm{h\,W\,m^{-2}}$) and relatively low CS ($< 0.5 \times 10^{-3}\mathrm{s^{-1}}$) are linked to more NPF days. Overall, the combinations of CS and solar insolation which promote NPF are relatively rare, compared to the entire set of measurements. In Fig. 8 the probability of occurrence (i.e. measurements linked to NPF day) is derived from the ratio of the number of measurements for each combination of CS and solar insolation during an NPF day to the number of valid data points for each of these combinations (where both sets of data are composed of hourly measurements) (see Sect. S10.1 for more details on the normalisation approach).

We define a region of interest (ROI) (represented using the red line, separating the top left-hand corner in Fig. 8). The ROI is defined using a simple straight line to separate ideal and non-ideal NPF conditions from each other. It should be stressed that it should not be used as an empirical relationship, defining the occurrence of NPF; instead it should be used as a guideline to highlight the general conditions most suitable for the promotion of NPF. In the ROI, the combination of low CS and plentiful solar insolation provides the most favourable conditions for NPF days to occur, and in contrast, outside of the ROI, NPF days are much less likely to occur (i.e. bottom right of Fig. 8).

Moreover, the region outside of the ROI with low solar insolation and low CS might be associated with increased cloudiness as the incident radiation is reduced by the presence of clouds, and large accumulation mode particles are reduced due to the effect of wet scavenging. The region with low solar insolation and high CS could be related to Arctic haze conditions.

The ROI defined in Fig. 8 is statistically significantly different from the non-ROI region on the probability that an NPF day occurs given such solar insolation and CS measurements occurring; the probabilities which arise when normalisation is done via the nanoranking classification scheme, as opposed to the Dal Maso et al. (2005) scheme, are more distinct between the ROI and non-ROI regions (see Fig. 9). Here, the statistical significance between the two regions is conducted using the non-parametric Mann–Whitney U test (where H_0 representing two identical distributions is rejected). In addition, the ROI and non-ROI represented 23 % and 77 % of the data, respectively; for the ROI 62.5 % of the hourly data were linked to NPF days, as opposed to 23.8 % in the non-ROI. (The total number of $\mathrm{Nano_{events}}$ is 229; g2 = 178, g3 = 51; see Fig. S16.)

The data points that lie within the ROI and when they occur can be used to try and estimate the likelihood of a day experiencing an NPF event. A time series representing the daily likelihood of NPF occurrence (i.e. $P_{\mathrm{NPF},D}$) can be generated from the ROI data (see Fig. 10) by labelling hourly data points as either 1 (i.e. within the ROI) or 0 (i.e. outside of the ROI) and then taking daily averages before applying a rolling average to create the daily likelihood, $P_{\mathrm{NPF},D}$. $P_{\mathrm{NPF},D}$ generally matches the frequency of NPF events as defined by Aliaga et al. (2023) or Dal Maso et al. (2005) (see Fig. 10); however, there are some major discrepancies. Generally, the predicted frequency of occurrence (i.e. defined by the ROI) is significantly lower than the observations (this can also be observed in the correlation in Fig. S28). The spring and autumn peaks in both $P_{\mathrm{NPF},D}$ and the event frequencies generally line up well in terms of the number of peaks; however, 2023 displays only one main peak in $P_{\mathrm{NPF},D}$. $P_{\mathrm{NPF},D}$ nicely replicates the distinctive dips in the NPF frequency before July in the years 2022 and 2024. However, in July 2023, the dip in NPF events in the observations is followed by an increase (i.e. two more sequential peaks in the observations) which is not captured by $P_{\mathrm{NPF},D}$. Still, it is striking that the two parameters alone (CS and solar insolation) are able to serve as predictors for NPF probability by representing the balance between the production and removal of NPF precursors. The solar insolation reflects the photochemical production potential (likely via the production of hydroxyl radicals). However, the parameter combination does not account for the reactants required to produce the nucleating vapours (which may be SO_2 (likely via DMS) and/or iodine compounds). Hence, deviations like those observed during July 2023 are expected as the conceptual model is partly incomplete due to a lack of adequate information regarding the original reactants. This said, however, the NPF frequency and likelihood largely seem limited by the balance between photochemical production potential and CS, and this in turn is suggestive of, to some degree, a self-regulating mechanism regarding the number of particles present in the nucleation and Aitken modes. It should be noted that there exist more sophisticated models to predict NPF (e.g. Kuang et al., 2010).

3.4.1 Ratio of source and sink: ratio of solar irradiance and condensation sink

In Sect, 4.1 we define a region of interest, whereby measurements within this ROI provide an indication of the conditions likely to lead to an NPF day. Observing when these conditions occur offers one approach; however, the ability to predict the occurrence of NPF days can be improved by sim-

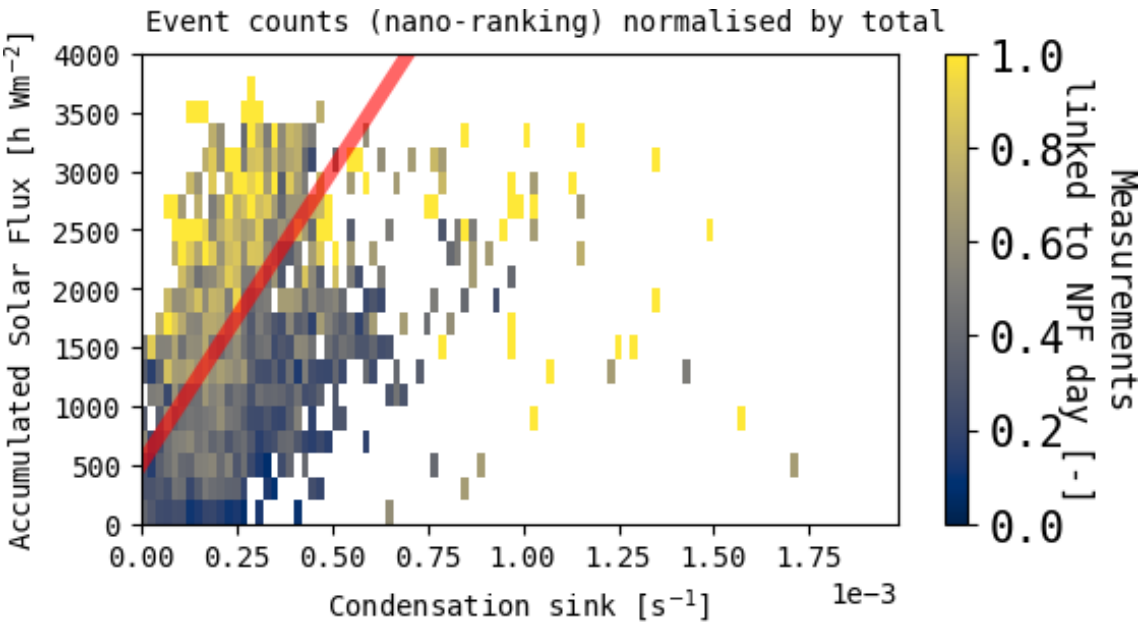

Figure 8. Grid mesh where the data are binned by accumulated solar insolation and condensation sink (CS) (CS between 0–10^{-3} s^{-1} every 2×10^{-5} s^{-1} and solar insolation between 0–4×10^{4} h W m^{-2} every 200 h W m^{-2}). Each grid box displays the likelihood, calculated by normalising the data set for the event days (defined using Aliaga et al., 2023) by the total count for each given bin (i.e. see Fig. S25a and b). Likelihood is the fraction of measurement combinations linked to an NPF day. The red line defines the region of interest (ROI), whereby data on the left of it are considered to have the ideal conditions for NPF, i.e. high accumulated solar flux and relatively low CS. The equation for the red line is solar insolation $= 5 \times 10^{6} \cdot \mathrm{CS} + 500$. The grid boxes required a count greater than 1.

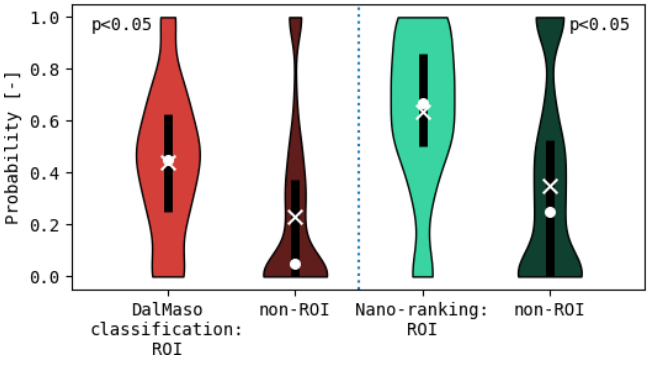

Figure 9. Violin plots representing the distribution of the probabilities as defined by the normalisation plot (see Fig. 8). The red violins on the left-hand side represent the probability distributions related to the Dal Maso et al. (2005) classification, and the green violins on the right-hand side represent the probability distributions according to the nano-ranking approach.

ply using the proxies for a source and a sink and taking their respective ratio (i.e. solar insolation/CS) (see Fig. 11). For a rolling average window of 30 d the R^2, comparing solar insolation/CS and the nano-ranking frequency, is 0.78 (see Fig. S26).

Figure 11 demonstrates that by using a simplified parameter, i.e. solar insolation/CS, albeit with a large rolling averaging window, we achieve a good agreement with both event frequencies (i.e. classified using the Dal Maso et al., 2005, or Aliaga et al., 2023, approach). There are some slight discrepancies between the solar insolation/CS parameter and the event frequencies, particularly at the start and end of the measurement period; the discrepancies could be due to the NPF seasons having started already or not having ended. The relationship between solar insolation/CS and event frequency varies depending on the averaging window utilised, whether the ML is selected, and also the type of classification used (see Fig. 12). The coefficient of determination (R^2) comparing solar insolation/CS and the daily event frequency (i.e. rolling average applied) increases and begins to plateau after a window of 2 weeks is applied (14 d, $R^2 = 0.65$) (see Fig. 12). Considering that a degree of averaging needs to be performed as the daily event frequencies are given as 1 s (event) and 0 s (non-event), it seems justified that the solar insolation/CS parameter offers a robust predictive capability once a modest amount of smoothing is performed.

3.5 Dynamics driving NPF and growth

During NPF events there is an excess availability of condensable precursors, e.g. SA, which contribute to the growth of newly formed and pre-existing particles, thus increasing CS. The increased CS enhances the removal of condensable and nucleating vapours. As a result, a typical day with sustained NPF can lead to a relatively high CS

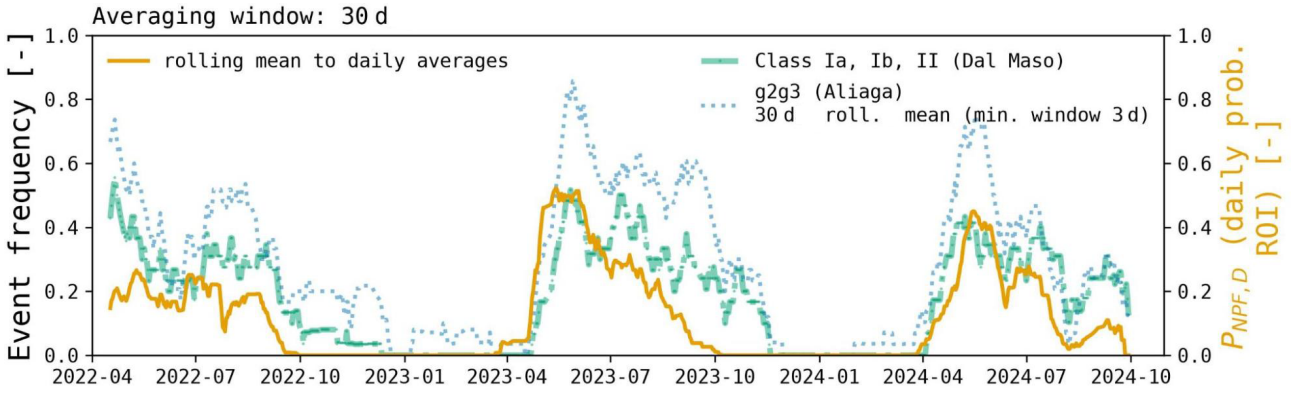

Figure 10. The orange line is $P_{\mathrm{NPF},D}$, the estimated daily likelihood of measurements occurring in the region of interest (ROI). The ROI is based on the relation between CS and 6 h solar accumulation and is defined in Fig. 8. The dash-dotted green and dotted blue lines represent the rolling averages of the NPF daily event frequencies using the Dal Maso et al. (2005) and Aliaga et al. (2023) classification, respectively. The green and blue curves are present here to be able to compare to $P_{\mathrm{NPF},D}$.

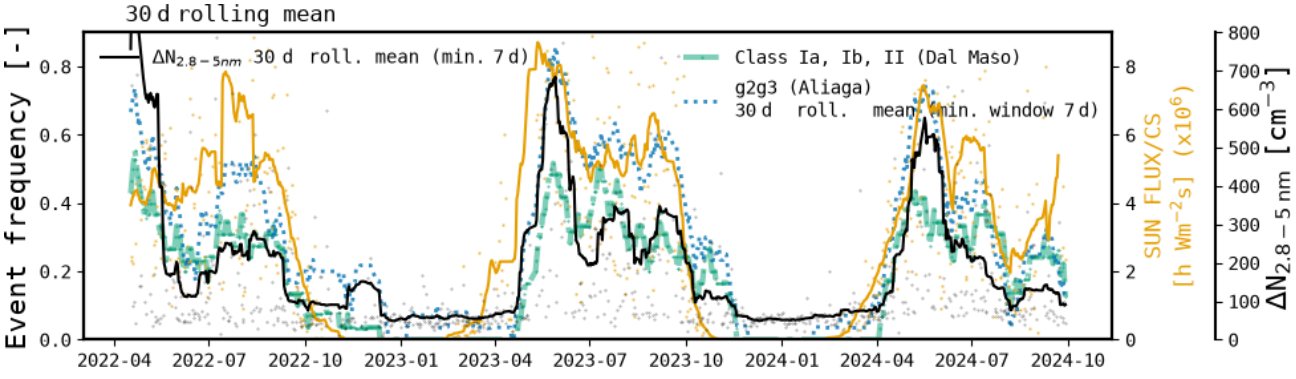

Figure 11. The solar insolation divided by the condensation sink (solar insolation/CS, SUN FLUX/CS) with a 30 d rolling mean is denoted by the orange line. The intensity parameter ($\Delta N_{2.8-5\,\mathrm{nm}}$) is shown in black. The dash-dotted green and dotted blue lines represent the rolling averages of the NPF daily event frequencies using the Dal Maso et al. (2005) and Aliaga et al. (2023) classification schemes, respectively. The green and blue curves are displayed to be able to compare to the orange line, the proxy for NPF activity, i.e. the balance between sources and sinks.

($> 0.5 \times 10^{-3}\,\mathrm{s}^{-1}$), although the events tend to begin at low CS values ($\sim 0.1 \times 10^{-3}\,\mathrm{s}^{-1}$) (see Fig. 13). It is worth noting that during an event, not only do the nucleation mode particles grow in size, but also all other existing particles grow as well. Practically, this means that the sink is doubled during the NPF event. Consequently, and assuming steady state, this would mean that the source rate of the condensing species must double to sustain the same concentration of condensing material.

The effect of this additional increase in CS during NPF events can be illustrated by using the ROI. The increase in CS shifts the ambient conditions away from the defined ROI ($> 0.5 \times 10^{-3}\,\mathrm{s}^{-1}$) (see Fig. 8), thus potentially suppressing any subsequent NPF events. This mechanism will prevent further NPF if the increase in CS during the NPF event is large enough to limit the availability of precursors. This mechanism also helps to explain why the combination of low CS and high solar insolation measurements are seemingly rare occurrences, as these conditions are soon followed by NPF and increasing CS.

During the Arctic haze period in late winter and early spring, high concentrations of accumulation mode aerosol dominate the contribution to the CS. Reduction in accumulation mode aerosol at the end of the Arctic haze season (i.e. end of May) should result in decreased CS, but ZEP continues to experience relatively high CS. We argue that this relatively high sustained CS is the result of particle formation and growth within the Arctic; the increasing frequency of NPF events during the summer months increases CS and maintains the comparatively high CS throughout the summer and the most intense part of the NPF season (see Fig. 2b as well as Tunved et al., 2013). Towards the late summer and autumn, the solar insolation has decreased substantially, and both marine surface water productivity and photochemical production potential are declining. Together with low transport efficiency from anthropogenic sources at lower latitudes

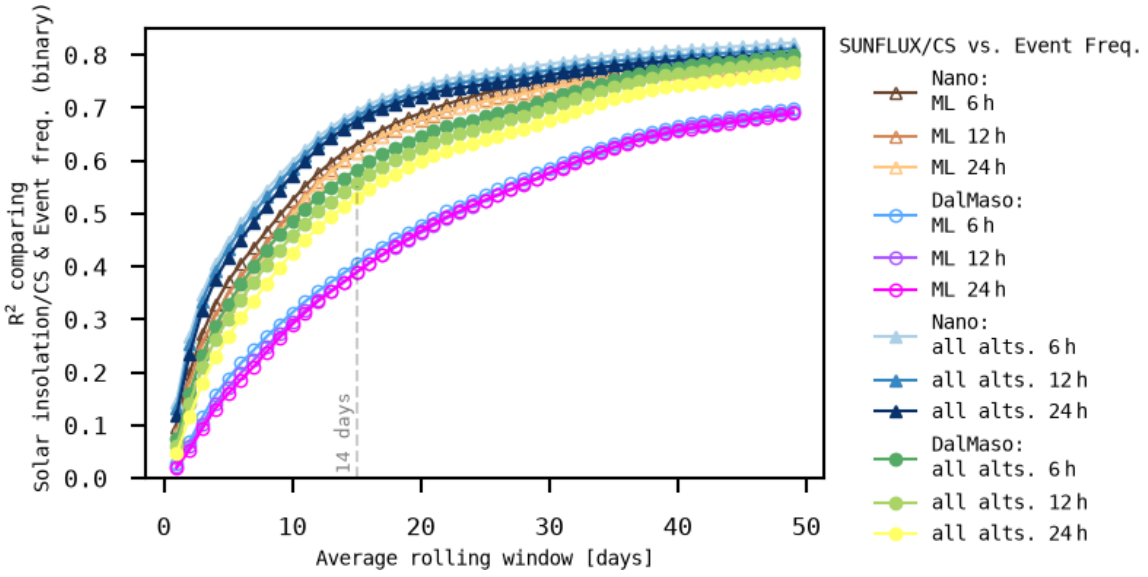

Figure 12. Correlation between the event frequency (defined using either the Dal Maso (circles) or nano-ranking (triangles) classification method) and the ratio of the accumulated solar insolation and CS (SUNFLUX/CS) with a rolling average applied. The coefficient of determination (R^2) is a function of the rolling window size (i.e. number of days). The first 6, 12, and 24 h of the back trajectories are selected (in different shades). The curve labelled ML (empty symbols) represents back trajectories that traversed only through the mixed layer, while the curves labelled "all alts." (whole symbols) represent back trajectories at all altitudes. Dashed grey line at 14 d to indicate plateauing of R^2.

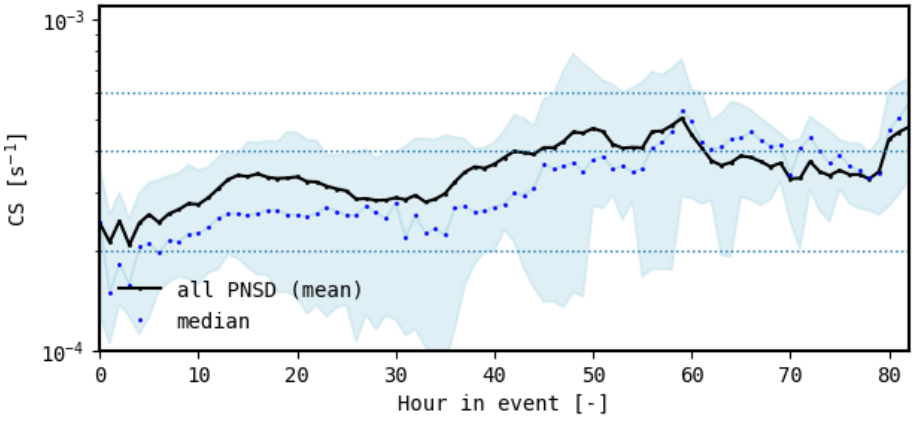

Figure 13. The calculated condensation sink (CS) during NPF events. It should be noted that the average NPF typically lasts for 10 h; however, in some cases events can persist for days until the newly formed mode is removed via wet scavenging or advected away from ZEP. The black line is the mean, and the blue is the median. The blue shaded region represents the 25th–75th percentiles. The dashed blue lines display CS values of 0.1, 0.2, and 0.4×10^{-3} s^{-1} and are there to guide the reader.

and efficient wet removal, the aerosol reaches a minimum with respect to CS and number during this part of the year.

In the Arctic environment, wet removal is a key factor responsible for the rapid reduction in CS (Garrett et al., 2011). For Class Ia and Ib NPF events, we can observe that prior to the start of an NPF event there is an increased likelihood of cloudy conditions (RH > 85 %) and rainfall events (see Fig. 14a–b). Figure 14a–b demonstrate how wet scavenging helps to effectively reduce the CS and provide more suitable conditions for NPF events to occur. The changes in the likelihood of cloudy conditions and rainfall prior to and after the start of an NPF event are slight, but significantly different, especially considering the duration prior to the event is longer, and the likelihood of any rainfall should be compounded.

Any reduction in CS will shift the system towards the ROI, and as a result the system will rapidly respond to this reduction by producing new particles and growing the already existing ones. If suitable gaseous precursors and solar insolation are present, NPF will take place, and the cycle will be reinitialised. This conceptual model, whilst highly simplified, offers substantial predictive value regarding the timing and frequency of NPF events (see Fig. 10). It does

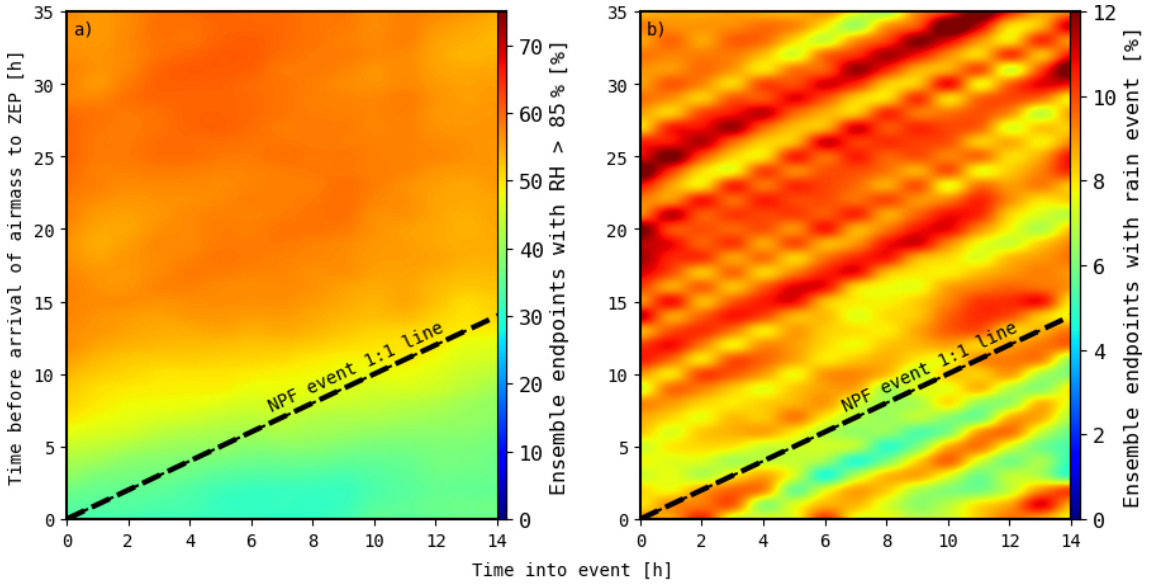

Figure 14. Air mass history for **(a)** percentage of back trajectory endpoints within an ensemble with a relative humidity above 85 and **(b)** percentage of endpoints within an ensemble which experienced a rainfall event (i.e. rainfall > 0 mm). The y axis is the number of hours backwards before the air masses arrive at ZEP, while the x axis is the number of hours into the event; e.g. if one event started at 06:00 and another at 09:00, their start times would both be 00:00. The black line is a 1 : 1 line which represents the start of the NPF event such that the grid points towards the top left represent endpoints prior to the NPF event, whilst grid points towards the bottom right represent endpoints during the NPF event. The x axis has been sliced based on the typical duration of events (most events are < 14 h). This figure consists of the air mass history of Class Ia and Ib NPF events.

not, however, account for the original source of condensable and nucleating species, nor does it consider cloud activation and the in-cloud chemistry of Aitken mode particles in non-precipitating clouds.

3.6 NPF contribution to Aitken and potential CCN

Here, we argue that new particle formation is the main contributor to the Aitken mode in the Arctic; through frequent NPF events and the subsequent growth of nucleation mode particles, NPF activity is able to provide a significant proportion of the overall concentration of Aitken mode particles. We show in Sect. 3.1.2 that at ZEP the production of nucleation mode particles is largest at the end of spring; however, the production of newly formed particles persists throughout the summer months and into the autumn (see Fig. 2a). During NPF events, including formation and subsequent growth, the total number concentration of Aitken mode particles (5–70 nm) is 3.6 times the amount compared with pre-event conditions (see Fig. 16). These events are relatively frequent (30 %–40 % of summer days experience NPF; see Fig. 1). Fundamentally, though, it is difficult to use in situ measurements at a single location to provide an estimation of the fraction of Aitken mode particles which are produced via NPF; for the Aitken mode particles at ZEP which are not directly linked to NPF activity, we cannot rule out the possibility that they are derived from NPF events outside of the vicinity of ZEP and then transported downwind.

At ZEP, NPF and the subsequent growth that follows result in particles large enough to potentially be activated and become CCN; on numerous occasions (57 times) we observed newly formed particles able to grow beyond 25 nm while in the same regional event (see Fig. 15b) before being scavenged. Here, we use 25 nm as the lowest bound for particles to act as CCN; however, it should be stated that this limit requires strong updrafts and extremely hygroscopic particles for particles to be activated. We observe that after ∼ 30 h of growth, we reach potential CCN sizes at ZEP (see Fig. 15a). In addition, on 11, 8, and 3 respective occasions NPF-produced particles were observed to grow beyond 60, 70, and 80 nm (see Fig. 15b). It is important to note that once produced these particles most likely continue to grow downwind of ZEP by condensation and in-cloud processing, so a large fraction of the Aitken mode should inevitably reach CCN size in due time, as long as they are not otherwise scavenged.

It is difficult to ascertain the proportion of NPF-derived Aitken mode particles that actually become CCN before being scavenged or deposited, and estimating an exact fraction is beyond the scope of this study. However, previous modelling and measurement studies can help to shed some light on the likelihood that NPF events as measured from ZEP can contribute to the CCN budget. Jung et al. (2018) demonstrate that at supersaturations (ss's) greater than 0.4 % there is a considerable number of CCN measured during the summer

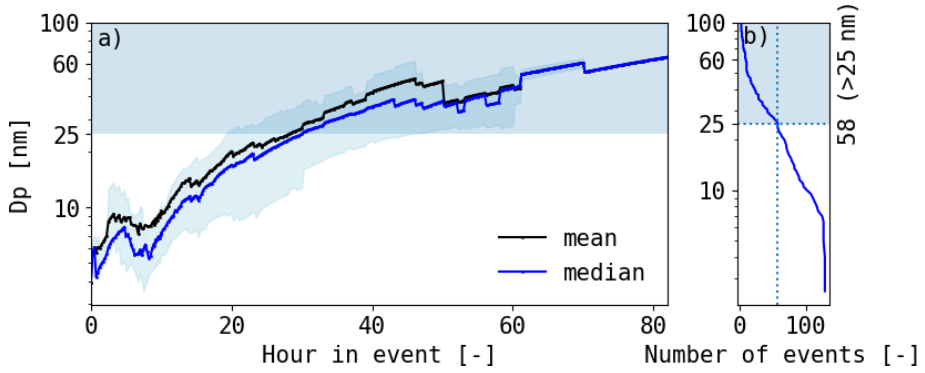

Figure 15. Change in diameter during all Class Ia, Ib, and II NPF events. The blue shaded region covers 25–60 nm. Panel **(a)** shows the average change in the diameter of the nucleation mode over time. The black and blue lines signify the mean and median diameters, respectively. The blue shaded region displays the distance between the 25th and 75th percentiles, respectively, and **(b)** displays the number of NPF events against the maximum diameter reached during growth. The horizontal dashed line marks 25 nm, whilst the vertical dashed line marks the number of NPF events which reached 25 nm.

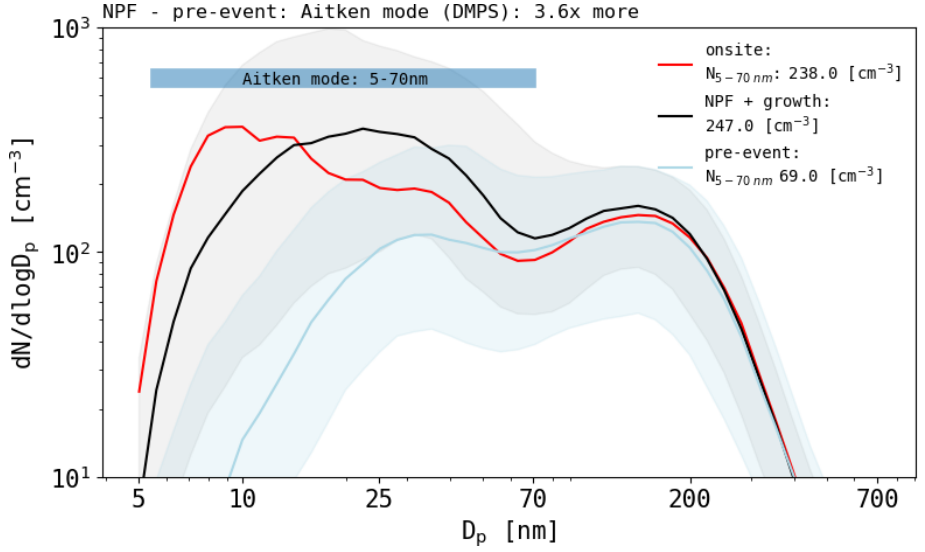

Figure 16. The particle number size distributions (DMPS) for periods before the NPF events (1–2 h before event started) (pre-event, light blue), during NPF and growth (black), and during on-site nucleation (production of 2–4 nm particles, red, *on-site formation*).

months at ZEP. Moreover, the changes in sources of CCN-sized aerosol particles, from mainly anthropogenic to NPF-derived, during the haze to summer transition can be seen in the reduction in the geometric mean diameter. For summer, Jung et al. (2018) suggest that a significant number of particles > 10 nm are activated into cloud droplets, as the activation ratio during summer is around 0.5 for fairly high ss, i.e. > 0.6 %. In addition, Karlsson et al. (2021) show that Aitken-mode-sized cloud residuals are fairly common in the summer time (i.e. July onwards); the transition from accumulation-mode-dominated to Aitken-mode-dominated aerosol did not lead to a significant reduction in the concentration of cloud residuals, indicating that particles as small as 20 nm can be activated. Motos et al. (2023) suggest that particles > 20 nm are activated in the summer, with a modal activation diameter of 60 nm showing that Aitken mode particles act as CCN.

4 Conclusion

In this study, we explore the annual cycle of atmospheric new particle formation (NPF) events from almost 3 years' worth of measurements (2022–2024). This study is the first to utilise the nano-ranking method in the Arctic. It should be stated that special care needs to be taken in treating wind-blown events separately from NPF events. Furthermore, this study also highlights potential problems when sampling lines are submerged in dense clouds. It is recommended that relative humidity, visibility, and/or web cam footage is used to help screen for these in-cloud events when sampling at high

altitudes. In keeping with previous studies, e.g. Tunved et al. (2013) and Ström et al. (2009), the Arctic summer and more specifically the end of spring and start of summer represent a peak in NPF intensity as observed at Zeppelin Observatory (ZEP). We find that this peak in the strength of NPF events coincides roughly with the maximum solar insolation (defined as the last 6 h of accumulated solar radiation along HYSPLIT back trajectories); solar insolation allows for the increased availability of precursors by encouraging oxidation. The NPF frequency during the summer remains fairly consistent, with an estimated 20 %–30 % of days experiencing an NPF event. Towards the end of summer, the decline in the amount of solar insolation reduces the NPF intensity. In addition, it is also apparent that the condensation sink (CS; i.e. linked to the total surface area of pre-existing aerosol) plays an important role, as the NPF intensity is more pronounced when there are reductions in CS. For NPF events, the minimum CS was observed at the start of the events and signifies that a reduced condensation sink is required for events to begin.

Typically, as the Arctic transitions from the haze season to summer, cloud coverage and precipitation increase, which in turn, via wet scavenging, reduces the once predominant accumulation mode. However, the increased cloud cover reduces not only the CS but also the solar insolation. Hence, the transition to summertime both promotes and discourages NPF. The latter stages of the summer and the autumn provide less solar insolation; the peak in solar insolation is skewed more towards the start of summer. These competing effects can explain why we observe such a reduction in NPF intensity as the summer progresses. The dip in frequency and intensity that occurs around July coincides with a decrease in brightness (solar insolation over potential solar radiation). It is the interplay between both solar insolation and condensation sink that can potentially give rise to NPF events, and thus cloudiness will also play a role in NPF activity given interplay with CS and solar radiation. We can only speculate that a warming climate may appear more similar to the late Arctic summer, being both warmer and wetter. Some studies indicate that cloud cover in the Arctic could potentially increase (Barton and Veron, 2012) or has (Eastman and Warren, 2010; Francis et al., 2009; Kay and Gettelman, 2009; Palm et al., 2010; Vihma et al., 2008) with periods of rapid sea ice loss.

One main finding from this study is that we can, with rather good accuracy, predict the occurrence of an NPF day (Fig. S26) by using CS and solar insolation as the two main predictive parameters. Periods exhibiting low CS and high solar insolation provide the most ideal conditions for NPF events, and the occurrence of these periods can reproduce the observed frequency of NPF events. It should be noted, though, that other factors play a role. The sources to the precursors of the condensable vapours, as well as additional meteorological and environmental parameters such as sea ice cover, chlorophyll *a* concentration, and the varying contributions from different source regions, all can influence the occurrence and strength of NPF. However, from this study we argue that both solar insolation and CS can be used to create a rather simple predictive model simply by taking the ratio of these two terms. The Arctic perhaps offers a unique environment, where the relationship between solar insolation and NPF is potentially stronger due to the typically lower CS and lower overall solar radiation intensity (Bousiotis et al., 2021).

Quantifying the contribution of CCN from NPF on low-level clouds is beyond the scope of this study. However, we are able to demonstrate that periods of formation and subsequent growth lead to a significant increase in the proportion of the total number of Aitken mode particles. In combination with this, we show that on many occasions during NPF events, the nucleation mode particles grow to potential CCN sizes once they are formed (57 NPF events lead to diameters > 25 nm). With the correct conditions, i.e. a relatively strong updraft, the formation of particles >25 nm could lead to droplet formation and in turn alter cloud properties.

Given the high frequency of on-site NPF and the large potential area for formation, it is not unlikely that a majority of Aitken mode particles originate from NPF within or close to the Arctic region. Provided sufficient time for growth up to CCN sizes, it seems clear that NPF events could constitute a significant source of CCN in the Arctic. For a more detailed picture of the aerosol budget in the Arctic and a more quantitative account of the NPF contribution to the overall Arctic CCN population, large-scale modelling evaluated against observations and combined with process studies is required.

Code availability. The code used to generate the figures presented in this study is available at https://doi.org/10.5281/zenodo.22695621 (dominichr1, 2026). The associated GitHub repository is available at https://doi.org/10.5281/zenodo.22695621 (dominichr1, 2026)).

Data availability. Data from this study will be available in the Bolin Centre Database.

Supplement. The supplement related to this article is available online at https://doi.org/10.5194/ar-4-457-2026-supplement.

Author contributions. DHR, RK, and PT worked together to develop the research questions and design the study. DHR performed data analysis and wrote the paper together with assistance from RK and PT. There was good input and advice along the way from IR, AK, DA, and MMi. JL developed many of the NAIS-specific Python packages and showed DHR how to clean and service the NAIS. SG provided comments. SG, MS, MMa, and RT helped with the Gruvabadet work. KTP and KT maintained and operated the Zeppelin DMS analyser as part of a collaborative effort between the

KOPRI and POSTECH research teams. KP and YJY provided the Nano SMPS data.

Competing interests. The contact author has declared that none of the authors has any competing interests.

Disclaimer. Publisher's note: Copernicus Publications remains neutral with regard to jurisdictional claims made in the text, published maps, institutional affiliations, or any other geographical representation in this paper. The authors bear the ultimate responsibility for providing appropriate place names. Views expressed in the text are those of the authors and do not necessarily reflect the views of the publisher.

Acknowledgements. This study would not be possible without the work done by the research engineers Birgitta Noone, Tabea Henning, and Ondrej Tesar from ACES and the staff from the Norwegian Polar Institute (NPI). The NPI provides invaluable on-site support including attending to the NAIS. The NPI is also acknowledged for substantial long-term support in maintaining the measurements at Zeppelin Observatory (ZEP). We would also like to thank Kai Rosman for developing the software we used for the instrumentation at ZEP. We would like to thank Ove Hermansen from the Norwegian Institute for Air Research (NILU) for providing the ambient meteorological data.

Financial support. Aerosol size distribution measurements are supported by the Swedish EPA. Swedish participation was supported by the Swedish Environmental Protection Agency's (Naturvårdsverket) environmental monitoring programme (Miljöövervakning), the Knut and Allice Wallenberg Foundation (KWA) within the Arctic Climate Across Scales (project no. 2016.0024), and the FORMAS funding agency ("Interplay between water, clouds and Aerosols in the Arctic" project; grant no. 2016-01427).

The aerosol observations at the Zeppelin station have been supported by the KAW Stiftelse (grant no. 2016.0024), the Swedish Environmental Protection agency (Naturvårdsverket), and the ACTRIS Sweden project supported by the Swedish Research Council.

The KAW project CLIVE and VR financed infrastructure project ACTRIS-Sweden.

Ilona Riipinen work was supported from EU MSCA Project 101073026–CLOUD-DOC.

Review statement. This paper was edited by Nad'a Zíková and reviewed by three anonymous referees.

References

Aliaga, D., Tuovinen, S., Zhang, T., Lampilahti, J., Li, X., Ahonen, L., Kokkonen, T., Nieminen, T., Hakala, S., Paasonen, P., Bianchi, F., Worsnop, D., Kerminen, V.-M., and Kulmala, M.: Nanoparticle ranking analysis: determining new particle formation (NPF) event occurrence and intensity based on the concentration spectrum of formed (sub-5 nm) particles, Aerosol Research, 1, 81–92, https://doi.org/10.5194/ar-1-81-2023, 2023.

Asmi, E., Kondratyev, V., Brus, D., Laurila, T., Lihavainen, H., Backman, J., Vakkari, V., Aurela, M., Hatakka, J., Viisanen, Y., Uttal, T., Ivakhov, V., and Makshtas, A.: Aerosol size distribution seasonal characteristics measured in Tiksi, Russian Arctic, Atmos. Chem. Phys., 16, 1271–1287, https://doi.org/10.5194/acp-16-1271-2016, 2016.

Baccarini, A., Karlsson, L., Dommen, J., Duplessis, P., Vüllers, J., Brooks, I. M., Saiz-Lopez, A., Salter, M., Tjernström, M., Baltensperger, U., Zieger, P., and Schmale, J.: Frequent new particle formation over the high Arctic pack ice by enhanced iodine emissions, Nat. Commun., 11, 4924, https://doi.org/10.1038/s41467-020-18551-0, 2020.

Barton, N. and Veron, D.: Response of clouds and surface energy fluxes to changes in sea-ice cover over the Laptev Sea (Arctic Ocean), Clim. Res., 54, 69–84, https://doi.org/10.3354/cr01101, 2012.

Beck, L. J., Sarnela, N., Junninen, H., Hoppe, C. J. M., Garmash, O., Bianchi, F., Riva, M., Rose, C., Peräkylä, O., Wimmer, D., Kausiala, O., Jokinen, T., Ahonen, L., Mikkilä, J., Hakala, J., He, X. C., Kontkanen, J., Wolf, K. K. E., Cappelletti, D., Mazzola, M., Traversi, R., Petroselli, C., Viola, A. P., Vitale, V., Lange, R., Massling, A., Nøjgaard, J. K., Krejci, R., Karlsson, L., Zieger, P., Jang, S., Lee, K., Vakkari, V., Lampilahti, J., Thakur, R. C., Leino, K., Kangasluoma, J., Duplissy, E. M., Siivola, E., Marbouti, M., Tham, Y. J., Saiz-Lopez, A., Petäjä, T., Ehn, M., Worsnop, D. R., Skov, H., Kulmala, M., Kerminen, V. M., and Sipilä, M.: Differing Mechanisms of New Particle Formation at Two Arctic Sites, Geophys. Res. Lett., 48, https://doi.org/10.1029/2020GL091334, 2021.

Bousiotis, D., Brean, J., Pope, F. D., Dall'Osto, M., Querol, X., Alastuey, A., Perez, N., Petäjä, T., Massling, A., Nøjgaard, J. K., Nordstrøm, C., Kouvarakis, G., Vratolis, S., Eleftheriadis, K., Niemi, J. V., Portin, H., Wiedensohler, A., Weinhold, K., Merkel, M., Tuch, T., and Harrison, R. M.: The effect of meteorological conditions and atmospheric composition in the occurrence and development of new particle formation (NPF) events in Europe, Atmos. Chem. Phys., 21, 3345–3370, https://doi.org/10.5194/acp-21-3345-2021, 2021.

Boyer, M., Aliaga, D., Quéléver, L. L. J., Bucci, S., Angot, H., Dada, L., Heutte, B., Beck, L., Duetsch, M., Stohl, A., Beck, I., Laurila, T., Sarnela, N., Thakur, R. C., Miljevic, B., Kulmala, M., Petäjä, T., Sipilä, M., Schmale, J., and Jokinen, T.: The annual cycle and sources of relevant aerosol precursor vapors in the central Arctic during the MOSAiC expedition, Atmos. Chem. Phys., 24, 12595–12621, https://doi.org/10.5194/acp-24-12595-2024, 2024.

Brean, J., Beddows, D. C. S., Harrison, R. M., Song, C., Tunved, P., Ström, J., Krejci, R., Freud, E., Massling, A., Skov, H., Asmi, E., Lupi, A., and Dall'Osto, M.: Collective geographical ecoregions and precursor sources driving Arctic new particle formation, Atmos. Chem. Phys., 23, 2183–2198, https://doi.org/10.5194/acp-23-2183-2023, 2023.

Cai, R. and Jiang, J.: A new balance formula to estimate new particle formation rate: reevaluating the effect of coag-

ulation scavenging, Atmos. Chem. Phys., 17, 12659–12675, https://doi.org/10.5194/acp-17-12659-2017, 2017.

Covert, D. S., Wiedensohler, A., Aalto, P., Heintzenberg, J., Mcmurry, P. H., and Leck, C.: Aerosol number size distributions from 3 to 500 nm diameter in the arctic marine boundary layer during summer and autumn, Tellus B, 48, 197–212, https://doi.org/10.3402/tellusb.v48i2.15886, 1996.

Croft, B., Martin, R. V., Leaitch, W. R., Tunved, P., Breider, T. J., D'Andrea, S. D., and Pierce, J. R.: Processes controlling the annual cycle of Arctic aerosol number and size distributions, Atmos. Chem. Phys., 16, 3665–3682, https://doi.org/10.5194/acp-16-3665-2016, 2016.

Dada, L., Chellapermal, R., Buenrostro Mazon, S., Paasonen, P., Lampilahti, J., Manninen, H. E., Junninen, H., Petäjä, T., Kerminen, V.-M., and Kulmala, M.: Refined classification and characterization of atmospheric new-particle formation events using air ions, Atmos. Chem. Phys., 18, 17883–17893, https://doi.org/10.5194/acp-18-17883-2018, 2018.

Dallósto, M., Beddows, D. C. S., Tunved, P., Krejci, R., Ström, J., Hansson, H. C., Yoon, Y. J., Park, K. T., Becagli, S., Udisti, R., Onasch, T., Ódowd, C. D., Simó, R., and Harrison, R. M.: Arctic sea ice melt leads to atmospheric new particle formation, Sci. Rep., 7, https://doi.org/10.1038/s41598-017-03328-1, 2017.

Dal Maso, M., Kulmala, M., Lehtinen, K. E. J., Mäkelä, J. M., Aalto, P., and O'Dowd, C. D.: Condensation and coagulation sinks and formation of nucleation mode particles in coastal and boreal forest boundary layers, J. Geophys. Res.-Atmos., 107, https://doi.org/10.1029/2001JD001053, 2002.

Dal Maso, M., Kulmala, M., Riipinen, I., Wagner, R., Hussein, T., Aalto, P. P., and Lehtinen, K. E. J.: Formation and growth of fresh atmospheric aerosols: eight years of aerosol size distribution data from SMEAR II, Hyytiälä, Finland, Boreal Environ. Res., 10, 323, https://doi.org/10.60910/yq6q-vj10, 2005.

dominichr1: ar-2025-11-v1.0.5 (Version v1.0.5), Zenodo [computer software], https://doi.org/10.5281/zenodo.22962960, 2026.

Draxler, R. R. and Hess, G. D.: An Overview of the HYSPLIT_4 Modelling System for Trajectories, Dispersion, and Deposition, Australian Meteorological Magazine, 47, 295–308, https://doi.org/10.1071/ES98032, 1998.

Eastman, R. and Warren, S. G.: Interannual variations of arctic cloud types in relation to sea ice, J. Climate, 23, 4216–4232, https://doi.org/10.1175/2010JCLI3492.1, 2010.

Fiedler, V., Dal Maso, M., Boy, M., Aufmhoff, H., Hoffmann, J., Schuck, T., Birmili, W., Hanke, M., Uecker, J., Arnold, F., and Kulmala, M.: The contribution of sulphuric acid to atmospheric particle formation and growth: a comparison between boundary layers in Northern and Central Europe, Atmos. Chem. Phys., 5, 1773–1785, https://doi.org/10.5194/acp-5-1773-2005, 2005.

Finkenzeller, H., Iyer, S., He, X.-C., et al.: The gas-phase formation mechanism of iodic acid as an atmospheric aerosol source, Nat. Chem., 15, 129–135, https://doi.org/10.1038/s41557-022-01067-z, 2023.

Francis, J. A., Chan, W., Leathers, D. J., Miller, J. R., and Veron, D. E.: Winter Northern Hemisphere weather patterns remember summer Arctic sea-ice extent, Geophys. Res. Lett., 36, https://doi.org/10.1029/2009GL037274, 2009.

Fuchs, N. A. and Sutugin, A. G.: Highly Dispersed Aerosols, Ann Arbor Science Publishers, Michigan, ISBN 9780250399963 , 1970.

Galí, M. and Simõ, R.: A meta-analysis of oceanic DMS and DMSP cycling processes: Disentangling the summer paradox, Global Biogeochem. Cy., 29, 496–515, https://doi.org/10.1002/2014GB004940, 2015.

Garrett, T. J. and Zhao, C.: Increased Arctic cloud longwave emissivity associated with pollution from mid-latitudes, Nature, 440, 787–789, https://doi.org/10.1038/nature04636, 2006.

Garrett, T. J., Zhao, C., Dong, X., Mace, G. G., and Hobbs, P. V.: Effects of varying aerosol regimes on low-level Arctic stratus, Geophys. Res. Lett., 31, https://doi.org/10.1029/2004GL019928, 2004.

Garrett, T. J., Brattström, S., Sharma, S., Worthy, D. E. J., and Novelli, P.: The role of scavenging in the seasonal transport of black carbon and sulfate to the Arctic, Geophys. Res. Lett., 38, https://doi.org/10.1029/2011GL048221, 2011.

Ghahreman, R., Gong, W., Galí, M., Norman, A.-L., Beagley, S. R., Akingunola, A., Zheng, Q., Lupu, A., Lizotte, M., Levasseur, M., and Leaitch, W. R.: Dimethyl sulfide and its role in aerosol formation and growth in the Arctic summer – a modelling study, Atmos. Chem. Phys., 19, 14455–14476, https://doi.org/10.5194/acp-19-14455-2019, 2019.

Gordon, H., Kirkby, J., Baltensperger, U., Bianchi, F., Breitenlechner, M., Curtius, J., Dias, A., Dommen, J., Donahue, N. M., Dunne, E. M., Duplissy, J., Ehrhart, S., Flagan, R. C., Frege, C., Fuchs, C., Hansel, A., Hoyle, C. R., Kulmala, M., Kürten, A., Lehtipalo, K., Makhmutov, V., Molteni, U., Rissanen, M. P., Stozkhov, Y., Tröstl, J., Tsagkogeorgas, G., Wagner, R., Williamson, C., Wimmer, D., Winkler, P. M., Yan, C., and Carslaw, K. S.: Causes and importance of new particle formation in the present-day and preindustrial atmospheres, J. Geophys. Res.-Atmos., 122, 8739–8760, https://doi.org/10.1002/2017JD026844, 2017.

Gormley, P. G. and Kennedy, M.: Diffusion from a Stream Flowing through a Cylindrical Tube, in: Proceedings of the Royal Irish Academy. Section A: Mathematical and Physical Sciences, 52, 163–169, 1948.

Gramlich, Y., Siegel, K., Haslett, S. L., Freitas, G., Krejci, R., Zieger, P., and Mohr, C.: Revealing the chemical characteristics of Arctic low-level cloud residuals – in situ observations from a mountain site, Atmos. Chem. Phys., 23, 6813–6834, https://doi.org/10.5194/acp-23-6813-2023, 2023.

Heintzenberg, J. and Leck, C.: The summer aerosol in the central Arctic 1991–2008: did it change or not?, Atmos. Chem. Phys., 12, 3969–3983, https://doi.org/10.5194/acp-12-3969-2012, 2012.

Hirsikko, A., Nieminen, T., Gagné, S., Lehtipalo, K., Manninen, H. E., Ehn, M., Hõrrak, U., Kerminen, V.-M., Laakso, L., McMurry, P. H., Mirme, A., Mirme, S., Petäjä, T., Tammet, H., Vakkari, V., Vana, M., and Kulmala, M.: Atmospheric ions and nucleation: a review of observations, Atmos. Chem. Phys., 11, 767–798, https://doi.org/10.5194/acp-11-767-2011, 2011.

Hoffmann, E. H., Tilgner, A., Schrödner, R., Bräuer, P., Wolke, R., and Herrmann, H.: An advanced modeling study on the impacts and atmospheric implications of multiphase dimethyl sulf ide chemistry, P. Natl. Acad. Sci. USA, 113, 11776–11781, https://doi.org/10.1073/pnas.1606320113, 2016.

Jang, E., Park, K.-T., Yoon, Y. J., Kim, T.-W., Hong, S.-B., Becagli, S., Traversi, R., Kim, J., and Gim, Y.: New particle formation events observed at the King Sejong Station, Antarctic Penin-

sula – Part 2: Link with the oceanic biological activities, Atmos. Chem. Phys., 19, 7595–7608, https://doi.org/10.5194/acp-19-7595-2019, 2019.

Jang, S., Park, K. T., Lee, K., and Suh, Y. S.: An analytical system enabling consistent and long-term measurement of atmospheric dimethyl sulfide, Atmos. Environ., 134, 217–223, https://doi.org/10.1016/j.atmosenv.2016.03.041, 2016.

Jokinen, T., Sipilä, M., Kontkanen, J., Vakkari, V., Tisler, P., Duplissy, E.-M., Junninen, H., Kangasluoma, J., Manninen, H. E., Petäjä, T., Kulmala, M., Worsnop, D. R., Kirkby, J., Virkkula, A., and Kerminen, V.-M.: Ion-induced sulfuric acid-ammonia nucleation drives particle formation in coastal Antarctica, Sci. Adv., 4, eaat9744, https://doi.org/10.1126/sciadv.aat9744, 2018.

Jung, C. H., Yoon, Y. J., Kang, H. J., Gim, Y., Lee, B. Y., Ström, J., Krejci, R., and Tunved, P.: The seasonal characteristics of cloud condensation nuclei (CCN) in the arctic lower troposphere, Tellus B, 70, 1–13, https://doi.org/10.1080/16000889.2018.1513291, 2018.

Kangasluoma, J., Cai, R., Jiang, J., Deng, C., Stolzenburg, D., Ahonen, L. R., Chan, T., Fu, Y., Kim, C., Laurila, T. M., Zhou, Y., Dada, L., Sulo, J., Flagan, R. C., Kulmala, M., Petäjä, T., and Lehtipalo, K.: Overview of measurements and current instrumentation for 1–10 nm aerosol particle number size distributions, J. Aerosol Sci., 148, 105584, https://doi.org/10.1016/j.jaerosci.2020.105584, 2020.

Karl, M., Leck, C., Gross, A., and Pirjola, L.: A study of new particle formation in the marine boundary layer over the central Arctic Ocean using a flexible multicomponent aerosol dynamic model, Tellus B, 64, https://doi.org/10.3402/tellusb.v64i0.17158, 2012.

Karlsson, L., Krejci, R., Koike, M., Ebell, K., and Zieger, P.: A long-term study of cloud residuals from low-level Arctic clouds, Atmos. Chem. Phys., 21, 8933–8959, https://doi.org/10.5194/acp-21-8933-2021, 2021.

Karlsson, L., Krejci, R., Koike, M., Ebell, K., and Zieger, P.: A long-term study of cloud residuals from low-level Arctic clouds, Atmos. Chem. Phys., 21, 8933–8959, https://doi.org/10.5194/acp-21-8933-2021, 2021.

Kay, J. E. and Gettelman, A.: Cloud influence on and response to seasonal Arctic sea ice loss, J. Geophys. Res.-Atmos., 114, https://doi.org/10.1029/2009JD011773, 2009.

Kecorius, S., Vogl, T., Paasonen, P., Lampilahti, J., Rothenberg, D., Wex, H., Zeppenfeld, S., van Pinxteren, M., Hartmann, M., Henning, S., Gong, X., Welti, A., Kulmala, M., Stratmann, F., Herrmann, H., and Wiedensohler, A.: New particle formation and its effect on cloud condensation nuclei abundance in the summer Arctic: a case study in the Fram Strait and Barents Sea, Atmos. Chem. Phys., 19, 14339–14364, https://doi.org/10.5194/acp-19-14339-2019, 2019.

Kerminen, V. M., Chen, X., Vakkari, V., Petäjä, T., Kulmala, M., and Bianchi, F.: Atmospheric new particle formation and growth: Review of field observations, Environ. Res. Lett., 13, 103003, https://doi.org/10.1088/1748-9326/aadf3c, 2018.

Kirkby, J., Curtius, J., Almeida, J., Dunne, E., Duplissy, J., Ehrhart, S., Franchin, A., Gagné, S., Ickes, L., Kürten, A., Kupc, A., Metzger, A., Riccobono, F., Rondo, L., Schobesberger, S., Tsagkogeorgas, G., Wimmer, D., Amorim, A., Bianchi, F., Breitenlechner, M., David, A., Dommen, J., Downard, A., Ehn, M., Flagan, R. C., Haider, S., Hansel, A., Hauser, D., Jud, W., Junninen, H., Kreissl, F., Kvashin, A., Laaksonen, A., Lehtipalo, K., Lima, J., Lovejoy, E. R., Makhmutov, V., Mathot, S., Mikkilä, J., Minginette, P., Mogo, S., Nieminen, T., Onnela, A., Pereira, P., Petäjä, T., Schnitzhofer, R., Seinfeld, J. H., Sipilä, M., Stozhkov, Y., Stratmann, F., Tomé, A., Vanhanen, J., Viisanen, Y., Vrtala, A., Wagner, P. E., Walther, H., Weingartner, E., Wex, H., Winkler, P. M., Carslaw, K. S., Worsnop, D. R., Baltensperger, U., and Kulmala, M.: Role of sulphuric acid, ammonia and galactic cosmic rays in atmospheric aerosol nucleation, Nature, 476, 429–435, https://doi.org/10.1038/nature10343, 2011.

Kirkby, J., Duplissy, J., Sengupta, K., Frege, C., Gordon, H., Williamson, C., Heinritzi, M., Simon, M., Yan, C., Almeida, J., Trostl, J., Nieminen, T., Ortega, I. K., Wagner, R., Adamov, A., Amorim, A., Bernhammer, A. K., Bianchi, F., Breitenlechner, M., Brilke, S., Chen, X., Craven, J., Dias, A., Ehrhart, S., Flagan, R. C., Franchin, A., Fuchs, C., Guida, R., Hakala, J., Hoyle, C. R., Jokinen, T., Junninen, H., Kangasluoma, J., Kim, J., Krapf, M., Kurten, A., Laaksonen, A., Lehtipalo, K., Makhmutov, V., Mathot, S., Molteni, U., Onnela, A., Perakyla, O., Piel, F., Petaja, T., Praplan, A. P., Pringle, K., Rap, A., Richards, N. A. D., Riipinen, I., Rissanen, M. P., Rondo, L., Sarnela, N., Schobesberger, S., Scott, C. E., Seinfeld, J. H., Sipila, M., Steiner, G., Stozhkov, Y., Stratmann, F., Tomé, A., Virtanen, A., Vogel, A. L., Wagner, A. C., Wagner, P. E., Weingartner, E., Wimmer, D., Winkler, P. M., Ye, P., Zhang, X., Hansel, A., Dommen, J., Donahue, N. M., Worsnop, D. R., Baltensperger, U., Kulmala, M., Carslaw, K. S., and Curtius, J.: Ion-induced nucleation of pure biogenic particles, Nature, 533, 521–526, https://doi.org/10.1038/nature17953, 2016.

Kolesar, K. R., Cellini, J., Peterson, P. K., Jefferson, A., Tuch, T., Birmili, W., Wiedensohler, A., and Pratt, K. A.: Effect of Prudhoe Bay emissions on atmospheric aerosol growth events observed in Utqiaġvik (Barrow), Alaska, Atmos. Environ., 152, 146–155, https://doi.org/10.1016/j.atmosenv.2016.12.019, 2017.

Kristensson, adam, Johansson, martin, swietlicki, erik, Kivekäs, niku, hussein, tareq, nieminen, tuomo, Kulmala, markku, and Dal maso, miikka: nanomap: Geographical mapping of atmospheric new-particle formation through analysis of particle number size distribution and trajectory data, Boreal Environ. Res., 19, 329–342, https://doi.org/10.60910/ypam-x33d , 2014.

Kuang, C., Riipinen, I., Sihto, S.-L., Kulmala, M., McCormick, A. V., and McMurry, P. H.: An improved criterion for new particle formation in diverse atmospheric environments, Atmos. Chem. Phys., 10, 8469–8480, https://doi.org/10.5194/acp-10-8469-2010, 2010.

Kulmala, M., Petäjä, T., Nieminen, T., Sipilä, M., Manninen, H. E., Lehtipalo, K., Dal Maso, M., Aalto, P. P., Junninen, H., Paasonen, P., Riipinen, I., Lehtinen, K. E. J., Laaksonen, A., and Kerminen, V. M.: Measurement of the nucleation of atmospheric aerosol particles, Nat. Protoc., 7, 1651–1667, https://doi.org/10.1038/nprot.2012.091, 2012.

Kulmala, M., Kontkanen, J., Junninen, H., Lehtipalo, K., Manninen, H. E., and Nieminen, T.: Direct Observations of Atmospheric Aerosol Nucleation, Science, 339, 943–946, https://doi.org/10.1126/science.1227385, 2013.

Leaitch, W. R., Sharma, S., Huang, L., Toom-Sauntry, D., Chivulescu, A., Macdonald, A. M., Von Salzen, K., Pierce, J. R., Bertram, A. K., Schroder, J. C., Shantz, N. C., Chang, R. Y. W., and Norman, A. L.: Dimethyl sulfide control of

the clean summertime Arctic aerosol and cloud, Elementa, 1, https://doi.org/10.12952/journal.elementa.000017, 2013.

Leaitch, W. R., Korolev, A., Aliabadi, A. A., Burkart, J., Willis, M. D., Abbatt, J. P. D., Bozem, H., Hoor, P., Köllner, F., Schneider, J., Herber, A., Konrad, C., and Brauner, R.: Effects of 20–100 nm particles on liquid clouds in the clean summertime Arctic, Atmos. Chem. Phys., 16, 11107–11124, https://doi.org/10.5194/acp-16-11107-2016, 2016.

Lee, H., Lee, K., Lunder, C. R., Krejci, R., Aas, W., Park, J., Park, K.-T., Lee, B. Y., Yoon, Y. J., and Park, K.: Atmospheric new particle formation characteristics in the Arctic as measured at Mount Zeppelin, Svalbard, from 2016 to 2018, Atmos. Chem. Phys., 20, 13425–13441, https://doi.org/10.5194/acp-20-13425-2020, 2020.

Lee, K., Kim, J. S., Park, K. T., Park, M. J., Jang, E., Gudmundsson, K., Olafsdottir, S. R., Olafsson, J., Yoon, Y. J., Lee, B. Y., Kwon, S. Y., and Kam, J.: Observational evidence linking ocean sulfur compounds to atmospheric dimethyl sulfide during Icelandic Sea phytoplankton blooms, Sci. Total Environ., 879, https://doi.org/10.1016/j.scitotenv.2023.163020, 2023.

Li, J., Carlson, B. E., Yung, Y. L., Lv, D., Hansen, J., Penner, J. E., Liao, H., Ramaswamy, V., Kahn, R. A., Zhang, P., Dubovik, O., Ding, A., Lacis, A. A., Zhang, L., and Dong, Y.: Scattering and absorbing aerosols in the climate system, Nature Reviews Earth & Environment, 3, 363–379, https://doi.org/10.1038/s43017-022-00296-7, 2022.

Manninen, H. E., Franchin, A., Schobesberger, S., Hirsikko, A., Hakala, J., Skromulis, A., Kangasluoma, J., Ehn, M., Junninen, H., Mirme, A., Mirme, S., Sipilä, M., Petäjä, T., Worsnop, D. R., and Kulmala, M.: Characterisation of corona-generated ions used in a Neutral cluster and Air Ion Spectrometer (NAIS), Atmos. Meas. Tech., 4, 2767–2776, https://doi.org/10.5194/amt-4-2767-2011, 2011.

Maturilli, M. and Ebell, K.: Twenty-five years of cloud base height measurements by ceilometer in Ny-Ålesund, Svalbard, Earth Syst. Sci. Data, 10, 1451–1456, https://doi.org/10.5194/essd-10-1451-2018, 2018.

Mauritsen, T., Sedlar, J., Tjernström, M., Leck, C., Martin, M., Shupe, M., Sjogren, S., Sierau, B., Persson, P. O. G., Brooks, I. M., and Swietlicki, E.: An Arctic CCN-limited cloud-aerosol regime, Atmos. Chem. Phys., 11, 165–173, https://doi.org/10.5194/acp-11-165-2011, 2011.

Merikanto, J., Spracklen, D. V., Mann, G. W., Pickering, S. J., and Carslaw, K. S.: Impact of nucleation on global CCN, Atmos. Chem. Phys., 9, 8601–8616, https://doi.org/10.5194/acp-9-8601-2009, 2009.

Mirme, A., Tamm, E., Mordas, G., Vana, M., Uin, J., Mirme, S., Bernotas, T., Laakso, L., Kulmala, M., and Hirsikko, A.: A wide-range multi-channel air ion spectrometer, Boreal Environ. Res., 12, 247–264, 2007.

Mirme, S. and Mirme, A.: The mathematical principles and design of the NAIS – a spectrometer for the measurement of cluster ion and nanometer aerosol size distributions, Atmos. Meas. Tech., 6, 1061–1071, https://doi.org/10.5194/amt-6-1061-2013, 2013.

Motos, G., Freitas, G., Georgakaki, P., Wieder, J., Li, G., Aas, W., Lunder, C., Krejci, R., Pasquier, J. T., Henneberger, J., David, R. O., Ritter, C., Mohr, C., Zieger, P., and Nenes, A.: Aerosol and dynamical contributions to cloud droplet formation in Arctic low-level clouds, Atmos. Chem. Phys., 23, 13941–13956, https://doi.org/10.5194/acp-23-13941-2023, 2023.

Nguyen, Q. T., Glasius, M., Sørensen, L. L., Jensen, B., Skov, H., Birmili, W., Wiedensohler, A., Kristensson, A., Nøjgaard, J. K., and Massling, A.: Seasonal variation of atmospheric particle number concentrations, new particle formation and atmospheric oxidation capacity at the high Arctic site Villum Research Station, Station Nord, Atmos. Chem. Phys., 16, 11319–11336, https://doi.org/10.5194/acp-16-11319-2016, 2016.

Nieminen, T., Kerminen, V.-M., Petäjä, T., Aalto, P. P., Arshinov, M., Asmi, E., Baltensperger, U., Beddows, D. C. S., Beukes, J. P., Collins, D., Ding, A., Harrison, R. M., Henzing, B., Hooda, R., Hu, M., Hõrrak, U., Kivekäs, N., Komsaare, K., Krejci, R., Kristensson, A., Laakso, L., Laaksonen, A., Leaitch, W. R., Lihavainen, H., Mihalopoulos, N., Németh, Z., Nie, W., O'Dowd, C., Salma, I., Sellegri, K., Svenningsson, B., Swietlicki, E., Tunved, P., Ulevicius, V., Vakkari, V., Vana, M., Wiedensohler, A., Wu, Z., Virtanen, A., and Kulmala, M.: Global analysis of continental boundary layer new particle formation based on long-term measurements, Atmos. Chem. Phys., 18, 14737–14756, https://doi.org/10.5194/acp-18-14737-2018, 2018.

Palm, S. P., Strey, S. T., Spinhirne, J., and Markus, T.: Influence of Arctic sea ice extent on polar cloud fraction and vertical structure and implications for regional climate, J. Geophys. Res.-Atmos., 115, https://doi.org/10.1029/2010JD013900, 2010.

Park, K. T., Lee, K., Kim, T. W., Yoon, Y. J., Jang, E. H., Jang, S., Lee, B. Y., and Hermansen, O.: Atmospheric DMS in the Arctic Ocean and Its Relation to Phytoplankton Biomass, Global Biogeochem. Cy., 32, 351–359, https://doi.org/10.1002/2017GB005805, 2018.

Pei, Q., Saikawa, E., Kaspari, S., Widory, D., Zhao, C., Wu, G., Loewen, M., Wan, X., Kang, S., Wang, X., Zhang, Y. L., and Cong, Z.: Sulfur aerosols in the Arctic, Antarctic, and Tibetan Plateau: Current knowledge and future perspectives, Earth-Sci. Rev., 220, 103753, https://doi.org/10.1016/j.earscirev.2021.103753, 2021.

Pirjola, L., O'Dowd, C. D., Brooks, I. M., and Kulmala, M.: Can new particle formation occur in the clean marine boundary layer?, J. Geophys. Res.-Atmos., 105, 26531–26546, https://doi.org/10.1029/2000JD900310, 2000.

Platt, S. M., Hov, Ø., Berg, T., Breivik, K., Eckhardt, S., Eleftheriadis, K., Evangeliou, N., Fiebig, M., Fisher, R., Hansen, G., Hansson, H.-C., Heintzenberg, J., Hermansen, O., Heslin-Rees, D., Holmén, K., Hudson, S., Kallenborn, R., Krejci, R., Krognes, T., Larssen, S., Lowry, D., Lund Myhre, C., Lunder, C., Nisbet, E., Nizzetto, P. B., Park, K.-T., Pedersen, C. A., Aspmo Pfaffhuber, K., Röckmann, T., Schmidbauer, N., Solberg, S., Stohl, A., Ström, J., Svendby, T., Tunved, P., Tørnkvist, K., van der Veen, C., Vratolis, S., Yoon, Y. J., Yttri, K. E., Zieger, P., Aas, W., and Tørseth, K.: Atmospheric composition in the European Arctic and 30 years of the Zeppelin Observatory, Ny-Ålesund, Atmos. Chem. Phys., 22, 3321–3369, https://doi.org/10.5194/acp-22-3321-2022, 2022.

Pöhlker, M. L., Zhang, M., Campos Braga, R., Krüger, O. O., Pöschl, U., and Ervens, B.: Aitken mode particles as CCN in aerosol- and updraft-sensitive regimes of cloud droplet formation, Atmos. Chem. Phys., 21, 11723–11740, https://doi.org/10.5194/acp-21-11723-2021, 2021.

Price, R., Baccarini, A., Schmale, J., Zieger, P., Brooks, I. M., Field, P., and Carslaw, K. S.: Late summer transition from a free-tropospheric to boundary layer source of Aitken mode aerosol in the high Arctic, Atmos. Chem. Phys., 23, 2927–2961, https://doi.org/10.5194/acp-23-2927-2023, 2023.

Quinn, P. K., Miller, T. L., Bates, T. S., Ogren, J. A., Andrews, E., and Shaw, G. E.: A 3-year record of simultaneously measured aerosol chemical and optical properties at Barrow, Alaska, J. Geophys. Res.-Atmos., 107, https://doi.org/10.1029/2001jd001248, 2002.

Schmale, J. and Baccarini, A.: Progress in Unraveling Atmospheric New Particle Formation and Growth Across the Arctic, Geophys. Res. Lett., 48, https://doi.org/10.1029/2021GL094198, 2021.

Schmale, J., Sharma, S., Decesari, S., Pernov, J., Massling, A., Hansson, H.-C., von Salzen, K., Skov, H., Andrews, E., Quinn, P. K., Upchurch, L. M., Eleftheriadis, K., Traversi, R., Gilardoni, S., Mazzola, M., Laing, J., and Hopke, P.: Pan-Arctic seasonal cycles and long-term trends of aerosol properties from 10 observatories, Atmos. Chem. Phys., 22, 3067–3096, https://doi.org/10.5194/acp-22-3067-2022, 2022.

Shaw, G. E.: The Arctic Haze Phenomenon, B. Am. Meteorol. Soc., 76, 2403–2414, https://doi.org/10.1175/1520-0477(1995)076<2403:TAHP>2.0.CO;2, 1995.

Stein, A. F., Draxler, R. R., Rolph, G. D., Stunder, B. J. B., Cohen, M. D., and Ngan, F.: Noaa's hysplit atmospheric transport and dispersion modeling system, B. Am. Meteorol. Soc., 96, 2059–2077, https://doi.org/10.1175/BAMS-D-14-00110.1, 2015.

Ström, J., Umegård, J., Tørseth, K., Tunved, P., Hansson, H. C., Holmén, K., Wismann, V., Herber, A., and König-Langlo, G.: One year of particle size distribution and aerosol chemical composition measurements at the Zeppelin Station, Svalbard, March 2000-March 2001, Phys. Chem. Earth, 28, 1181–1190, https://doi.org/10.1016/j.pce.2003.08.058, 2003.

Ström, J., Engvall, A. C., Delbart, F., Krejci, R., and Treffeisen, R.: On small particles in the Arctic summer boundary layer: Observations at two different heights near Ny-Ålesund, Svalbard, Tellus B, 61, 473–482, https://doi.org/10.1111/j.1600-0889.2008.00412.x, 2009.

Tammet, H., Komsaare, K., and Hõrrak, U.: Intermediate ions in the atmosphere, Atmos. Res., 135–136, 263–273, https://doi.org/10.1016/j.atmosres.2012.09.009, 2014.

Tunved, P., Ström, J., and Krejci, R.: Arctic aerosol life cycle: linking aerosol size distributions observed between 2000 and 2010 with air mass transport and precipitation at Zeppelin station, Ny-Ålesund, Svalbard, Atmos. Chem. Phys., 13, 3643–3660, https://doi.org/10.5194/acp-13-3643-2013, 2013.

Vihma, T., Jaagus, J., Jakobson, E., and Palo, T.: Meteorological conditions in the Arctic Ocean in spring and summer 2007 as recorded on the drifting ice station Tara, Geophys. Res. Lett., 35, https://doi.org/10.1029/2008GL034681, 2008.

von der Weiden, S.-L., Drewnick, F., and Borrmann, S.: Particle Loss Calculator – a new software tool for the assessment of the performance of aerosol inlet systems, Atmos. Meas. Tech., 2, 479–494, https://doi.org/10.5194/amt-2-479-2009, 2009.

Wagner, R., Manninen, H. E., Franchin, A., Lehtipalo, K., Mirme, S., Steiner, G., Petäjä, T., and Kulmala, M.: On the accuracy of ion measurements using a Neutral cluster and Air Ion Spectrometer, Boreal Environ. Res., 21, 230–241, https://doi.org/10.60910/xr8j-5a1a, 2016.

Wagner, R., Yan, C., Lehtipalo, K., Duplissy, J., Nieminen, T., Kangasluoma, J., Ahonen, L. R., Dada, L., Kontkanen, J., Manninen, H. E., Dias, A., Amorim, A., Bauer, P. S., Bergen, A., Bernhammer, A.-K., Bianchi, F., Brilke, S., Mazon, S. B., Chen, X., Draper, D. C., Fischer, L., Frege, C., Fuchs, C., Garmash, O., Gordon, H., Hakala, J., Heikkinen, L., Heinritzi, M., Hofbauer, V., Hoyle, C. R., Kirkby, J., Kürten, A., Kvashnin, A. N., Laurila, T., Lawler, M. J., Mai, H., Makhmutov, V., Mauldin III, R. L., Molteni, U., Nichman, L., Nie, W., Ojdanic, A., Onnela, A., Piel, F., Quéléver, L. L. J., Rissanen, M. P., Sarnela, N., Schallhart, S., Sengupta, K., Simon, M., Stolzenburg, D., Stozhkov, Y., Tröstl, J., Viisanen, Y., Vogel, A. L., Wagner, A. C., Xiao, M., Ye, P., Baltensperger, U., Curtius, J., Donahue, N. M., Flagan, R. C., Gallagher, M., Hansel, A., Smith, J. N., Tomé, A., Winkler, P. M., Worsnop, D., Ehn, M., Sipilä, M., Kerminen, V.-M., Petäjä, T., and Kulmala, M.: The role of ions in new particle formation in the CLOUD chamber, Atmos. Chem. Phys., 17, 15181–15197, https://doi.org/10.5194/acp-17-15181-2017, 2017.

Wiedensohler, A., Covert, D. S., Swietlicki, E., Aalto, P., Heintzenberg, J., and Leck, C.: Occurrence of an ultrafine particle mode less than 20 nm in diameter in the marine boundary layer during Arctic summer and autumn, Tellus B, 48, 213–222, https://doi.org/10.3402/tellusb.v48i2.15887, 1996.

Willis, M. D., Leaitch, W. R., and Abbatt, J. P. D.: Processes Controlling the Composition and Abundance of Arctic Aerosol, Rev. Geophys., 56, 621–671, https://doi.org/10.1029/2018RG000602, 2018.

Xavier, C., Wollesen de jonge, R., Jokinen, T., Beck, L., Sipilä, M., Olenius, T., and Roldin, P.: Role of Iodine-Assisted Aerosol Particle Formation in Antarctica, Environ. Sci. Technol., 58, 7314–7324, https://doi.org/10.1021/acs.est.3c09103, 2024.

Yu, F. and Turco, R. P.: From molecular clusters to nanoparticles: Role of ambient ionization in tropospheric aerosol formation, J. Geophys. Res.-Atmos., 106, 4797–4814, https://doi.org/10.1029/2000JD900539, 2001.

Ziemba, L. D., Dibb, J. E., Griffin, R. J., Huey, L. G., and Beckman, P.: Observations of particle growth at a remote, Arctic site, Atmos Environ, 44, 1649–1657, https://doi.org/10.1016/j.atmosenv.2010.01.032, 2010.